

# Design and Development of a Cosmic Ray Detector and Data Dispatcher (CR3D)

---



Presented by:  
Zuhayr Halday

Prepared for:  
Assoc. Prof. S. Winberg  
Dept. of Electrical and Electronics Engineering  
University of Cape Town

Submitted to the Department of Electrical Engineering at the University of Cape Town  
in partial fulfillment of the academic requirements for a Bachelor of Science degree in  
Electrical and Computer Engineering

October 28, 2025



# Plagiarism Declaration

---

1. I know that plagiarism is wrong. Plagiarism is to use another's work and pretend that it is one's own.
2. I have used the IEEE convention for citation and referencing. Each contribution to, and quotation in, this report from the work(s) of other people has been attributed, and has been cited and referenced.
3. This report is my own work and is in my own words (except where I have attributed it to others).
4. I have not paid a third party to complete my work on my behalf. My use of artificial intelligence software has been limited to: minor report writing and argument structuring assistance, code debugging, and word counting.
5. I have not allowed and will not allow anyone to copy my work with the intention of passing it off as his or her own work.
6. I acknowledge that copying someone else's assignment or essay, or part of it, is wrong, and declare that this is my own work.

Signature: 

Z. Halday

Word Count: 14,749

Date: **October 28, 2025**

## Acknowledgments

---

I would like to acknowledge my parents first and foremost. I am profoundly grateful to you for your unwavering love, countless sacrifices, and steady belief in my success. You always remind me that despite my failures and shortcomings, I am still capable of so much more than I tend to give myself credit for. Thank you for opening the door to higher education and for standing behind every step that brought me here.

To my girlfriend, Nihaad: thank you for your constant encouragement, patience, and for picking me up whenever I'm down. You have always been my biggest supporter and the reason I strive to do my best every day. My journey through this degree has not been an easy one, and I would have never progressed so far in my studies if it wasn't for you.

I would also like to acknowledge Dr James Keaveney and Malefetsane Lenka of the UCT Physics Department's Muon Lab and UCT-CERN Research Centre for their generous loans of scintillators and equipment after my severe struggle to source these, and for their invaluable advice throughout this project. Their generosity, expert guidance and practical assistance made a decisive difference to the feasibility of this study.

# Abstract

---

This project presents the design and development of the *Cosmic Ray Detector and Data Dispatcher* (CR3D), a compact, educationally oriented muon-detection framework integrating simulation, analog signal processing, and modular data acquisition. Due to limitations in time, budget, and component availability, the project adopted a simulation-driven methodology that demonstrated the full detection chain without requiring empirical flux measurement. A Geant4 model of a plastic EJ-200 scintillator coupled to an SiPM was used to quantify photon yield responses to muon excitation. An analog front-end comprising a transimpedance amplifier, peak-hold, and low-pass filter was analytically designed and validated through LTSpice simulation and bench current-injection testing. An Arduino and Python-based firmware–GUI system enabled real-time plotting and structured logging of detector outputs. Results confirm that simulation can effectively substitute early-stage scintillator measurements, the analog front-end meets its speed, signal-shaping and bandwidth targets, and the acquisition software performs reliably, forming a scalable foundation for future coincidence detection and muon flux studies.

# Contents

<b>1</b>	<b>Introduction</b>	<b>1</b>
1.1	Background to the study . . . . .	1
1.2	Objectives of this study . . . . .	2
1.2.1	Problems to be investigated . . . . .	2
1.2.2	Purpose of the study . . . . .	2
1.3	Scope and Limitations . . . . .	2
1.4	Plan of Development . . . . .	3
<b>2</b>	<b>Literature Review</b>	<b>4</b>
2.1	Cosmic radiation . . . . .	4
2.1.1	Nature and origin of cosmic rays . . . . .	5
2.1.2	Characteristics and Influencing Factors of Sea-Level Muon Flux . . . . .	6
2.1.3	Particle interactions with matter . . . . .	7
2.1.4	Muon Counting . . . . .	9
2.2	Muon Detection . . . . .	11

2.2.1	Scintillation Detectors . . . . .	11
2.2.2	Cherenkov Detectors . . . . .	12
2.2.3	Ionization-Based Gas Detectors . . . . .	13
2.3	Readout photodetectors: SiPMs vs PMTs . . . . .	13
2.3.1	Operating principles . . . . .	13
2.3.2	Spectral Coupling to Plastic Scintillators . . . . .	14
2.3.3	Gain and Noise Mechanisms . . . . .	14
2.3.4	Environmental Sensitivities . . . . .	15
2.3.5	Implications for a Desk-Scale Muon Counter . . . . .	15
2.4	Software and simulation tools for modeling cosmic-ray interactions . . . .	15
2.4.1	Air-shower and surface-source generators . . . . .	16
2.4.2	Transport Through Matter and Detector Response . . . . .	16
2.4.3	Optical-Photon Simulation in Geant4 . . . . .	17
2.5	Related Open Designs: CosmicWatch and CosmicPi . . . . .	18
2.5.1	CosmicWatch . . . . .	18
2.5.2	CosmicPi . . . . .	19
2.6	Conclusion of Literature Review . . . . .	19
<b>3</b>	<b>Design Methodology and Theoretical Framework</b>	<b>21</b>
3.1	Overview of Methodological Approach . . . . .	21

3.1.1	Revised Research and Design Workflow . . . . .	22
3.1.2	Revised Project Goals and Scope . . . . .	23
3.2	Geant4 Scintillator Simulation Subsystem Design . . . . .	23
3.2.1	Overview of the Geant4 Simulation Framework . . . . .	24
3.2.2	Simulation Workflow and Event Handling . . . . .	24
3.2.3	Physics Model Selection and Energy Deposition . . . . .	26
3.2.4	Material Definitions and Scintillator Optical Properties . . . . .	26
3.2.5	Geometry and Boundary Conditions . . . . .	27
3.2.6	Photon Detection and Event Tracking . . . . .	27
3.2.7	Simulation Outputs and Observable Parameters . . . . .	28
3.2.8	Overall Subsystem Design . . . . .	28
3.3	Analog Front-End (AFE) Subsystem Design . . . . .	29
3.3.1	Literature-Informed Circuit Design . . . . .	30
3.3.2	Derived AFE Performance Requirements . . . . .	30
3.3.3	Component Evaluation and Selection . . . . .	31
3.3.4	Analytical Derivation of Passive Component Values . . . . .	33
3.3.5	Hardware Implementation and Experimental Constraints . . . . .	37
3.3.6	Acceptance Testing Matrix . . . . .	38
3.3.7	Overall Subsystem Design . . . . .	39
3.4	Firmware and Data-Logging Subsystem Design . . . . .	39



3.4.1	Design Objectives and Role within the System . . . . .	40
3.4.2	Microcontroller Selection and Justification . . . . .	40
3.4.3	Firmware Design . . . . .	41
3.4.4	Python Logger and GUI Design . . . . .	42
3.4.5	Overall Subsystem Design . . . . .	45
3.5	Conclusion of Design Methodology . . . . .	45
<b>4</b>	<b>Simulation/Design Testing and Results</b>	<b>46</b>
4.1	Scintillator Simulation Subsystem . . . . .	46
4.1.1	Test 1: Scintillation Outputs vs. Muon Energy . . . . .	46
4.1.2	Test 2: Scintillation Outputs vs. Muon Path Length . . . . .	48
4.1.3	Test 3: Scintillation Outputs vs. Birks' Constant . . . . .	49
4.2	Analog Front-End (AFE) Subsystem . . . . .	49
4.2.1	Simulated Circuit Testing . . . . .	50
4.2.2	Hardware Testing . . . . .	50
4.2.3	Acceptance Testing Results . . . . .	50
4.3	Firmware and Data-Logging Subsystem . . . . .	51
4.3.1	Live Operation and Serial Communication . . . . .	52
4.3.2	Graphical User Interface and Live Statistics . . . . .	52
4.3.3	Data Logging and File Output Verification . . . . .	53

<b>5</b>	<b>Discussion and Interpretation of Results</b>	<b>54</b>
5.1	Scintillator Simulation Subsystem . . . . .	54
5.1.1	Scintillation Outputs vs. Muon Energy . . . . .	54
5.1.2	Scintillation Outputs vs. Muon Path Length . . . . .	55
5.1.3	Scintillation Outputs vs. Birks' Constant . . . . .	55
5.2	Analog Front-End (AFE) Subsystem . . . . .	56
5.2.1	Simulated Circuit Testing . . . . .	56
5.2.2	Hardware Testing . . . . .	56
5.3	Firmware and Data-Logging Subsystem . . . . .	57
5.3.1	Live Operation and Serial Communication . . . . .	57
5.3.2	Graphical User Interface and Live Statistics . . . . .	57
5.3.3	Data Logging and File Output Verification . . . . .	57
5.4	Overall Discussion and Evaluation . . . . .	58
<b>6</b>	<b>Conclusions</b>	<b>59</b>
6.1	Alignment with Revised Goals . . . . .	59
6.2	Methodological and Scientific Contributions . . . . .	60
6.3	Overall Conclusions . . . . .	60
<b>7</b>	<b>Future Recommendations</b>	<b>62</b>
<b>A</b>	<b>Additional Files</b>	<b>68</b>

A.1	GitHub Repository Link . . . . .	68
A.2	GA Appendix . . . . .	69
A.3	Use of Artificial Intelligence Tools . . . . .	70
<b>B</b>	<b>Addenda</b>	<b>71</b>
B.1	Ethics Form . . . . .	71

# List of Figures

2.1	Representation of decay and interaction chains resulting from primary particle showers. <i>Adapted from</i> [1] . . . . .	5
2.2	EJ-200 plastic scintillator slab used in UCT’s Muon Lab . . . . .	11
3.1	Simplified UML class diagram of the Geant4 simulation. . . . .	25
3.2	3D interactive visualization of the simulated EJ-200 scintillator and SiPM window in <b>Geant4</b> . . . . .	29
3.3	Physical EJ-200 rods from UCT’s Muon Lab (with and without reflective wrapping). . . . .	29
3.4	KiCAD Schematic of the final AFE circuit. . . . .	36
3.5	Toner transfer and ferric chloride PCB etching process. . . . .	37
3.6	KiCAD SiPM PCB Design (left) in comparison to final etched PCB (right). . . . .	38
3.7	Final hardware-prototyped AFE circuit. . . . .	38
3.8	Simplified Arduino firmware logic flow. . . . .	42
3.9	Layout of the <code>cr3d_logger.py</code> graphical interface. . . . .	44
4.1	Visual output from Geant4 energy-sweep macro showing muon tracks (red) and scintillation photon emission (cyan) within the EJ-200 volume. . . . .	47

4.2	Simulation output showing relationship between muon energy and photons counts. . . . .	47
4.3	Visualization of muon trajectories producing different path lengths within the scintillator and its effect on photon yield. . . . .	48
4.4	Simulation output showing relationship between muon path length and photons counts. . . . .	48
4.5	Variation of photon yield with Birks' constant over the range 0.01–0.20 mm/MeV. . . . .	49
4.6	LTSpice transient simulation showing input current (pink), TIA output voltage (green), and final filtered output (cyan) of the AFE circuit. . . . .	50
4.7	Oscilloscope capture of TIA output (green) and AFE output voltage (yellow). . . . .	51
4.8	Example of live serial data stream showing alternating <b>sample</b> and <b>event</b> JSON messages received by the Python logger. . . . .	52
4.9	Graphical user interface of the Python data-logging application during active current-injection testing. . . . .	52
B.1	eRA Ethics Approval Form . . . . .	72

# List of Tables

3.1	Comparison of original and revised project goals and scope. . . . .	23
3.2	Derived performance targets for the AFE subsystem. . . . .	31
3.3	Comparison of candidate SiPM devices. . . . .	32
3.4	Comparison of candidate op-amps for the TIA stage. . . . .	32
3.5	Comparison of operational amplifiers evaluated for the peak-detection stage.	33
3.6	Acceptance test matrix for AFE subsystem. . . . .	39
3.7	Comparison of candidate microcontrollers for data acquisition. . . . .	40
4.1	Acceptance test results for the AFE subsystem. . . . .	51
4.2	Excerpt of recorded event data from logging subsystem. . . . .	53

# Chapter 1

## Introduction

### 1.1 Background to the study

Cosmic rays, high-energy particles originating from astrophysical sources such as supernovae and active galactic nuclei, continuously bombard the Earth's atmosphere. Upon collision with atmospheric nuclei, these primary cosmic rays generate cascades of secondary particles, among which muons are the most abundant at ground level. Muons are highly penetrative, long-lived charged particles that can traverse substantial thicknesses of matter, making them valuable probes for scientific and engineering applications such as particle physics experiments, geological surveying, and environmental radiation studies.

In recent years, the development of compact and low-cost muon detectors has enabled these investigations to move beyond large-scale facilities such as CERN and into educational, research, and even citizen-science contexts. Open-source projects have demonstrated that portable detectors can effectively record cosmic muon flux and serve as tools for both physics education and environmental monitoring. However, the design and calibration of such detectors remain non-trivial and requires an understanding of both the underlying particle interactions and the engineering trade-offs involved.

## 1.2 Objectives of this study

### 1.2.1 Problems to be investigated

The primary problem addressed in this study is how to develop a cost-effective, portable muon detector that maintains scientific reliability and measurement accuracy comparable to more sophisticated systems.

### 1.2.2 Purpose of the study

The purpose of this project is to demonstrate that meaningful cosmic-ray muon detection can be achieved with a compact, educationally oriented system using modern low-cost photodetectors and microcontrollers. By doing so, the project will provide an accessible platform that can be used for undergraduate research and science communication. The design process of such a system will serve as a practical exercise in multidisciplinary engineering, combining aspects of nuclear physics, optoelectronics, and software design.

## 1.3 Scope and Limitations

The scope of this project is restricted to the design, construction, and testing of a singular desktop-scale muon detector prototype capable of measuring muon counts. The detector will focus on the detection and counting of minimum-ionizing muons. Energy spectroscopy, particle identification beyond muons, and advanced geographical muon flux analysis are considered beyond the current scope. The prototype should be tested under laboratory and open-sky conditions to evaluate its detection efficiency, signal integrity, and stability.

Limitations include resource constraints such as time, budget, and access to specialized laboratory equipment. Environmental factors such as temperature fluctuations and background radiation are acknowledged but will not be controlled for beyond standard calibration procedures.



## 1.4 Plan of Development

This report is organized to reflect the logical progression of the detector's development from conceptual research to validated design. Chapter 2 presents a review of existing literature on cosmic radiation, muon detection, and relevant detector technologies. Chapter 3 outlines the complete design methodology, detailing the development of each subsystem and the integrated detection framework. Chapter 4 describes the testing procedures applied to each subsystem and presents the resulting data. Chapter 5 discusses and interprets these results in the context of theoretical expectations and design objectives. Finally, Chapters 6 and 7 present the project's conclusions and recommendations for future refinement and experimental validation.

# Chapter 2

## Literature Review

### How this review is organized

The structure of this review follows the logical progression from the underlying physics of cosmic radiation to the practical engineering considerations that inform detector design. It begins by outlining the origin and behavior of cosmic-ray muons at the Earth's surface, establishing the physical context within which a compact detector must operate. The discussion then turns to the mechanisms of particle detection, critically evaluating competing approaches in terms of efficiency, practicality, and educational scalability. Subsequent sections examine the role of particle simulation and modeling in predicting detector performance. Finally, recent open-source detector initiatives are reviewed to situate this project within the broader landscape of accessible scientific instrumentation. These sections aim to build a coherent argument for the design choices that may advance the development of a desktop muon detector.

### 2.1 Cosmic radiation

Cosmic radiation forms the ultimate source of the secondary muons detected at the Earth's surface [2]. Understanding its composition, interaction mechanisms, and resulting flux at ground level is fundamental to designing a reliable muon detector. The following review traces the origin of cosmic rays, their interaction with the atmosphere, and the properties of the resulting muon flux relevant to small-scale detection systems.

### 2.1.1 Nature and origin of cosmic rays

Cosmic rays comprise a spectrum of high-energy particles that reach Earth from space, with primary particle showers originating from both galactic and extragalactic sources [3]. This spectrum is dominated by protons, with helium nuclei and heavier ions contributing smaller fractions [4]. A representation of the various particle interaction chains leading to the production of secondary muons can be seen in Figure 2.1. When these primaries enter Earth's upper atmosphere, their collisions with atmospheric nuclei generate cascades of secondary particles that eventually produce muons at the ground level [2, 5]. This distinction is crucial: while primaries possess energies far beyond the detection capabilities of a bench-top experiment, the ground-level muon flux (arising from pion and kaon decays) represents the observable signature accessible to compact cosmic ray detectors.

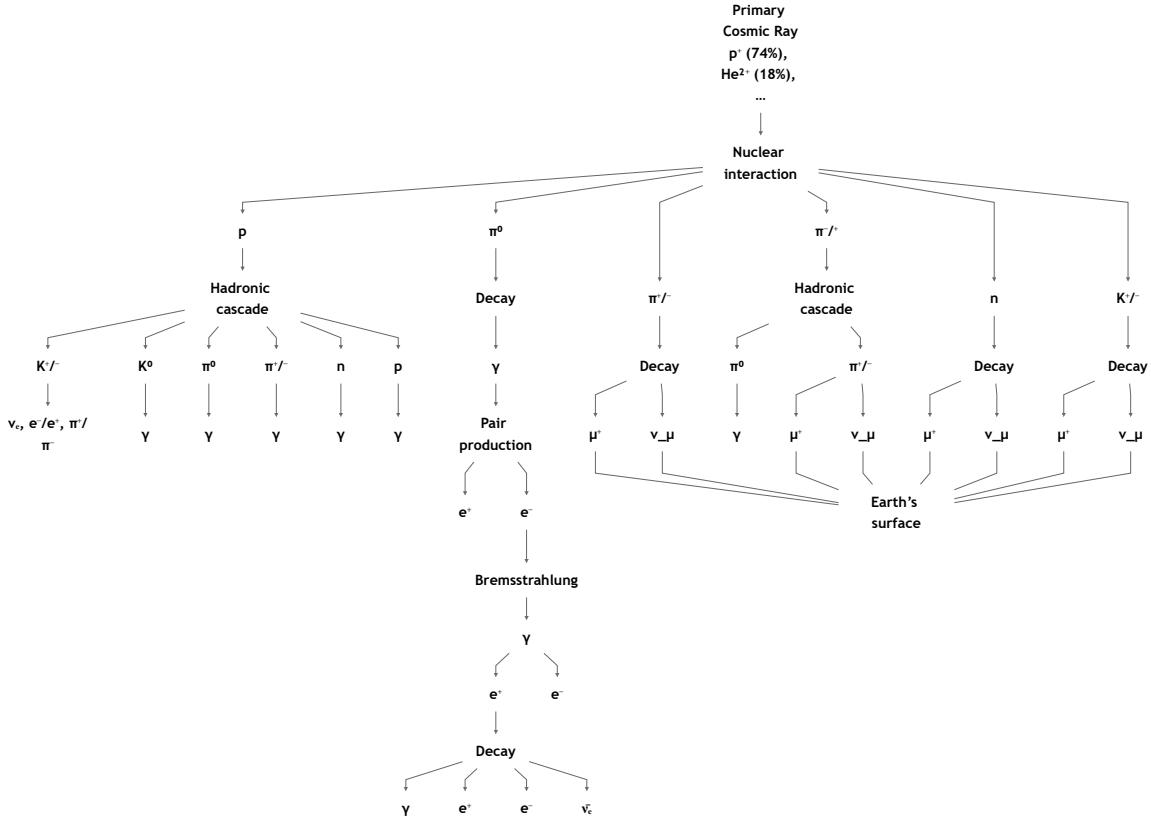


Figure 2.1: Representation of decay and interaction chains resulting from primary particle showers. *Adapted from* [1]

#### Primary particles: composition and energy spectrum

The all-particle spectrum approximately follows a power law  $J(E) \propto E^{-\gamma}$  that reflects particle acceleration and propagation [2, 5]. These features define the energy window for

secondary particle production in the atmosphere. The energies of ground-level muons therefore represent a filtered subset of the primary spectrum. For detector design, this relationship can illustrate constraints on expected muon energy levels, event rates, and the choice of materials capable of efficiently detecting these particles.

### **Air-shower development and secondary muon production**

When a high-energy primary particle enters the atmosphere, it initiates a nuclear cascade that produces mesons, mainly pions ( $\pi^\pm$ ) and kaons ( $K^\pm$ ), which subsequently decay into muons ( $\mu^\pm$ ) and neutrinos. The balance between meson decay and secondary particle re-interaction governs the resulting muon flux [2]. Muons travel at relativistic speeds while being roughly 207x heavier than electrons, meaning they are less prone to energy loss in matter and therefore capable of reaching sea level and even penetrating the Earth's crust [2, 6]. These surface-reaching muons possess mean energies between 1-5 GeV and lose minimal energy through ionization en route [5]. Since the probability of interaction increases with air density, only those mesons that decay before significant re-interaction contribute to detectable muons. This understanding dictates that cosmic ray detectors must be optimized for the efficient detection of minimum-ionizing muons: the most abundant and experimentally accessible component of the secondary cosmic radiation field.

### **2.1.2 Characteristics and Influencing Factors of Sea-Level Muon Flux**

The surface or sea-level muon flux provides the quantitative foundation for estimating count rates and designing the acceptance geometry of a small detector.

#### **Differential and integral flux at sea level**

At sea level, the vertical muon intensity is approximately  $70 \text{ m}^{-2} \text{ s}^{-1} \text{ sr}^{-1}$ , equivalent to roughly one particle per square centimeter per minute incident on a horizontal surface [2]. The differential energy spectrum steepens with increasing energy as meson re-interaction suppresses high-energy muon production. Thus, desk-scale detectors with tens of  $\text{cm}^2$  active area can accumulate statistically useful counts on minute timescales, provided its geometrical acceptance is not overly restrictive.

### Zenith-angle dependence

Muon intensity decreases with increasing zenith angle, well described by an empirical  $\cos^n \theta$  dependence, where  $n = 2$  for the few-GeV energy spectrum [2]. A more accurate relationship,

$$I(p_\mu, \theta) \simeq \cos^3 \theta I_v(p_\mu \cos \theta),$$

(where  $p_\mu$  is muon momentum,  $\theta$  the zenith angle,  $I(\cdot)$  a differential intensity, and  $I_v$  its vertical counterpart) relates off-vertical intensities to the vertical differential spectrum [7]. Put simply, muons arriving from overhead are more common than those skimming the horizon because the latter traverse more air and are more likely to lose energy before reaching a detector. This angular dependence defines the effective acceptance angle of a detector.

### Environmental and situational factors

The muon rate at the surface is also affected by variations in atmospheric pressure and temperature. An increase in surface pressure increases the overlying air column, reducing the observed flux, while higher stratospheric temperatures lengthen meson decay paths, slightly enhancing muon intensity [2]. Consequently, accurate muon rate interpretation requires constant measurement of environmental parameters such as pressure and temperature. For imaging applications such as muography, calibration under open-sky conditions using identical geometry is essential to establish a reliable reference flux [8].

### 2.1.3 Particle interactions with matter

Understanding how muons and other charged particles deposit energy in detector materials underpins every aspect of signal shaping, threshold setting, and background suppression for a small-scale detector.

#### Ionization vs. excitation; stopping-power concepts

For relativistic muons traversing matter, the dominant interaction process is ionization and excitation of atomic electrons. The mean energy loss per unit path length is well

described by the Bethe equation:

$$\left\langle -\frac{dE}{dx} \right\rangle = K z^2 \frac{Z}{A} \frac{1}{\beta^2} \left[ \frac{1}{2} \ln \left( \frac{2m_e c^2 \beta^2 \gamma^2 W_{\max}}{I^2} \right) - \beta^2 - \frac{\delta(\beta\gamma)}{2} \right],$$

where  $K$  is a proportionality constant,  $z = 1$  for muons, and  $(Z, A)$  are the target detector material parameters [6]. For minimum-ionizing muons, the stopping power reaches a shallow minimum around a few GeV, corresponding to an energy loss of roughly  $2 \text{ MeV } g^{-1} \text{ cm}^2$ . In small or thin detectors, this means that the amount of energy muons can deposit within the detector material will ultimately plateau around  $2 \text{ MeV } g^{-1} \text{ cm}^2$  even as kinetic energy increases [6].

### Cross-sections, mean free path, and interaction probability

The probability that a muon or secondary particle interacts within a given material depends on the microscopic interaction cross-section  $\sigma(E, Z, A)$ . The mean free path

$$\lambda = 1/(N\sigma) = M/(\rho N_A \sigma)$$

defines the average distance a particle travels before interaction [9]. For muons at GeV-scale energies, interaction cross-sections in low- $Z$  materials are extremely small, resulting in long mean free paths. Structural materials such as aluminum or acrylic enclosures therefore effectively appear transparent to muons, provided they remain thin. This implies that a detector housing or light-tight wrapping should minimize unnecessary material above the scintillator, as excessive thicknesses can reduce acceptance.

### Scintillation mechanism and quenching in plastics

When charged particles lose energy through ionization in an appropriate detector material, a fraction of that energy is converted into scintillation photons via excitation and de-excitation of the detectors molecular states. The relationship between deposited energy and emitted photons is governed by Birks' law:

$$\frac{dL}{dx} = \frac{S(dE/dx)}{1 + k_B(dE/dx)},$$

where  $S$  is the scintillation efficiency and  $k_B$  the quenching parameter, or Birks' constant [10]. For common commercially available polyvinyltoluene-based scintillators such as EJ-200, empirical studies suggest  $k_B \sim 10^{-2} \text{ g cm}^{-2} \text{ MeV}^{-1}$  [10, 11]. This quenching

effect becomes significant for heavily ionizing particles, whereas muons, being minimum-ionizing, remain within the near-linear regime. Optical-photon detector simulations and threshold optimization should therefore incorporate Birks' quenching to ensure accurate modeling of the light yield and to predict plateau behavior under varying conditions.

### **Other ionizing backgrounds**

Environmental background radiation can produce Compton electrons and recoil protons within scintillator detectors [12]. However, coincidence techniques effectively suppress these events. Coincidence detection requires simultaneous detection in two vertically aligned detector materials. Applying conservative thresholds, non-muon triggers can be reduced to negligible levels [11]. Without multiple detectors operating in coincidence however, it is near impossible to distinguish muon events from these possible non-muon triggers in a single detector.

#### **2.1.4 Muon Counting**

Beyond serving as a simple measure of cosmic-ray intensity, muon counting provides a versatile diagnostic. A scintillation telescope can be used not only to monitor flux variations and environmental dependencies but also to demonstrate muon decay physics and perform basic muographic imaging.

### **Flux monitoring and environmental correlations**

Discussed in section 2.1.2, surface-level muon count rate varies predictably with changes in barometric pressure and atmospheric temperature. Compact detectors such as two-slab telescopes reproduce these variations on daily and seasonal timescales, validating both stability and sensitivity. This quantitative relationship can be a key diagnostic of detector performance, but requires constant detection over long periods of time [13].

### **Muon lifetime and decay demonstrations**

Muon decay experiments form a cornerstone of undergraduate and small-scale physics research programs. When a positive muon stops within the scintillator, it decays and

produces a delayed positron signal. The observed decay time distribution follows an exponential law,  $N(t) = N_0 e^{-t/\tau_\mu}$  where the muon lifetime is  $\tau_\mu \approx 2.2\mu s$  [14]. By time-stamping the prompt stop signal and subsequent decay pulse, one can extract  $\tau_\mu$  with undergraduate-lab precision [15]. Although, these timing studies do necessitate the use of more complex muon detectors and would not be achievable by a small-scale detector.

### **Muon radiography (muography)**

Muon radiography exploits the directional attenuation of muon flux through dense objects. The technique compares the intensity of muons transmitted through a target,  $I_{\text{obj}}(\theta, \phi)$  to an open-sky  $I_{\text{open}}(\theta, \phi)$  yielding the transmission ratio:

$$T(\theta, \phi) = \frac{I_{\text{obj}}(\theta, \phi)}{I_{\text{open}}(\theta, \phi)},$$

with smaller  $T$  indicating a higher integrated density along the muon path [16]. Although most muography applications employ large-area detectors, the same principles could be demonstrated on a small scale using extremely well-characterized acceptance and open-sky reference measurements [7, 13].

### **Cosmic-ray effects on ground level electronics**

At ground level, the primary radiation-induced electronic effects stem not from muons themselves but from atmospheric neutrons produced in the associated cosmic-ray cascades [17]. These can cause transient single-event upsets (SEUs) in digital components, characterized by the soft error rate (SER):

$$\text{SER} = \int \Phi_n(E) \sigma_{\text{SEU}}(E) dE,$$

where  $\Phi_n(E)$  is the neutron flux and  $\sigma_{\text{SEU}}(E)$  the device's upset cross-section [18].

While these effects are rare, they can perturb long-duration performance of IC's or embedded electronics components in the form of spontaneous bit-flips and data corruption [18]. Muon counting could therefore be used to better quantify the relationship between overall cosmic-ray cascades and SER.



## 2.2 Muon Detection

Detecting cosmic muons at ground level requires converting the passage of a minimum-ionizing charged particle into a measurable, time-resolved electrical signal. Several detector classes can achieve this through distinct physical and material processes.

### 2.2.1 Scintillation Detectors

#### Organic plastic scintillators

Among the available options, plastic polyvinyltoluene (PVT) or polystyrene (PS) scintillators offer the most balanced performance for small-scale muon detection. Their fast nanosecond-scale emission, high light yield, and mechanical robustness make them well suited to compact geometries [19, 11]. A passing muon deposits energy into the scintillator by ionizing/exciting the polymer, and this excitation transfers to fluorescent organic dopants that promptly de-excite and emit visible photons [20].

Compared to liquid scintillators, solid plastics avoid containment and handling issues while maintaining similar photon yields. Against inorganic crystals, they are lighter, faster, and significantly cheaper per unit area. And unlike gaseous detectors, they require no high-voltage drift systems or gas maintenance. For this reason, a two-slab plastic telescope with each tile coupled to a photosensor and operated in coincidence has emerged as a practical standard for desktop muon-counting systems such as *CosmicWatch* [21].



Figure 2.2: EJ-200 plastic scintillator slab used in UCT’s Muon Lab

### Organic liquid scintillators and WbLS

While liquid scintillators provide flexible geometries and high photon yields, their advantages diminish sharply at small volumes. Linear alkylbenzene (LAB) and related liquid cocktails, as well as newer water-based liquid scintillators (WbLS), exhibit longer decay components and reduced light output per unit path length compared to plastics [22].

In laboratory-scale setups such as the LAGUNA European design study, liquid scintillation offers benefits in the way of good optical transport in bulk volumes and higher energy particle detection [23]. On a smaller scale however, light collection is further limited by attenuation and boundary losses, producing broader pulse-height distributions and lower signal-to-noise ratios. These characteristics necessitate more complex containment, monitoring, and maintenance than a bench-top detector warrants.

### Inorganic crystal scintillators

Inorganic scintillators such as NaI:Tl, CsI:Tl, BGO, or LYSO exhibit superior intrinsic light yields and radiation hardness but are generally slower and much more expensive than their organic counterparts [24, 25]. Their high atomic numbers improve efficiency for gamma detection but offer little benefit for relativistic muons, which deposit energy primarily via ionization rather than radiative processes [24].

For small-area, wide-acceptance detectors, the drawbacks of crystal scintillators include weight, cost, and hygroscopicity, which outweigh their advantages. Their longer decay times also complicate coincidence timing.

#### 2.2.2 Cherenkov Detectors

Cherenkov detectors provide exceptional timing resolution by exploiting the prompt emission of Cherenkov light when charged particles traverse a dielectric medium faster than light propagates within it. The emitted photon yield per unit length however, is limited by the refractive index of the medium and its volume [14, 26].

In small geometries, such as water or acrylic cells a few centimeters thick, photon statistics become marginal, making signal discrimination extremely sensitive and prone to noise [27]. While their intrinsic timing precision is unmatched, their low photon yield and

stringent mechanical requirements render them less robust for general-purpose, portable use.

### 2.2.3 Ionization-Based Gas Detectors

Gas detectors have been extensively developed for large-area muon tracking systems, such as the HERA-B detector in Germany [28]. These detectors rely on ionization of a gas volume followed by electron drift and avalanche multiplication, providing high spatial resolution and long-term stability [14].

However, the infrastructure demands pressurized gas systems, continuous flow control, and high-voltage operation, which introduce significant overhead. For small-scale, low-rate applications, the precision they offer is disproportionate to their complexity.

## 2.3 Readout photodetectors: SiPMs vs PMTs

The performance of any scintillation detector ultimately depends on the coupling between the scintillator and its photodetector. Photomultiplier tubes (PMTs) and silicon photomultipliers (SiPMs) emerge as the two dominant technologies.

### 2.3.1 Operating principles

PMTs and SiPMs achieve photon-to-electron conversion through fundamentally different mechanisms.

A PMT uses a bialkali photocathode to release photoelectrons that are amplified through a dynode chain, yielding high gains with sub-nanosecond transit-time spreads [29]. This electron multiplication process produces high-gain ( $10^6$ - $10^7$ ) and clean, quantized pulses even for single photons, though it requires high-voltage biasing (typically 1-2 kV) and careful shielding from magnetic fields.

An SiPM, by contrast, consists of thousands of avalanche photodiode (APD) microcells operating in Geiger mode. Each microcell discharges a fixed charge when triggered, with overall signal amplitude proportional to the number of fired cells. The gain is given by

$Q_{cell} = C_{cell}\Delta V$ , where  $C_{cell}$  is cell capacitance and  $\Delta V$  is the over-voltage above the stated breakdown voltage (unique to each model of SiPM) [30].

This solid-state architecture provides comparable gain to PMTs but at far lower voltages (typically 20–60 V). Thus, while PMTs remain unmatched in sensitivity under controlled laboratory conditions, SiPMs excel in environments demanding compactness, low power, and ease of integration at the circuit-board level.

### 2.3.2 Spectral Coupling to Plastic Scintillators

Efficient optical coupling requires spectral overlap between the scintillator’s emission and the photodetector’s photon detection efficiency (PDE). The emission spectra of plastic EJ-200 and EJ-204 scintillators peak in the blue–violet region (around 425 nm wavelength), coinciding well with the response of both bialkali PMTs and blue-enhanced SiPMs [19, 29].

While a PMT’s PDE is fixed by its photocathode material, an SiPM’s PDE varies with applied over-voltage. This adjustability allows fine-tuning between efficiency and correlated noise.

### 2.3.3 Gain and Noise Mechanisms

The two technologies differ markedly in their intrinsic noise characteristics.

PMTs exhibit extremely low dark noise, limited primarily by thermionic emission from the photocathode [29]. SiPMs, on the other hand, experience thermally generated carriers, afterpulsing, and optical crosstalk between adjacent microcells. These effects scale with both temperature and over-voltage [30].

In a single-channel system, these differences can be significant, which is why accurate muon flux measurements in these systems is unattainable. In coincidence-based muon telescopes however, uncorrelated noise is suppressed by orders of magnitude, effectively neutralizing SiPM disadvantages.

### 2.3.4 Environmental Sensitivities

PMTs and SiPMs exhibit distinct environmental dependencies. PMTs are largely immune to temperature variation but are highly sensitive to magnetic fields, which can distort electron trajectories in the dynode chain [29]. SiPMs, conversely, are unaffected by magnetic fields but display temperature-dependent breakdown voltages, requiring gain stabilization either through active bias compensation or periodic recalibration [30].

### 2.3.5 Implications for a Desk-Scale Muon Counter

Considering performance, practicality, and integration, SiPMs represent the most appropriate choice for a portable, low-cost muon counter. They offer compactness, low-voltage operation, and excellent timing at minimal infrastructure overhead.

PMTs retain advantages in specialized contexts requiring ultra-low noise, larger photocathode areas, or existing HV systems, but for a standalone educational or research-grade instrument, the SiPM provides an optimal balance of performance, simplicity, and safety. The adoption of SiPM readout therefore aligns with the broader design philosophy established in this review, favoring modularity, low power, and accessibility without compromising data fidelity.

## 2.4 Software and simulation tools for modeling cosmic-ray interactions

A realistic understanding of muon flux, detector response, and systematic uncertainty requires more than analytical or mathematical models. Computational simulations enable the generation of realistic particle fields, the transport of these particles through materials, and the prediction of detector observables under specific geometrical and environmental conditions. For a small-scale muon telescope, an efficient simulation framework will be crucial in validating expected photon emissions and muon counts.

### 2.4.1 Air-shower and surface-source generators

#### CRY (Cosmic-Ray Shower Library)

The Cosmic-Ray Shower Library (CRY) is a C++ based library that provides precomputed correlations between the positions, directions, energies, and timing of secondary cosmic-ray particles at selectable altitudes [31]. For sea-level studies, it serves as a convenient and physically validated surface source generator, capable of sampling muons, neutrons, and other secondaries consistent with experimental measurements.

CRY's compact implementation and existing interfaces to other toolkits such as Geant4 make it particularly suited to educational and prototype-scale detector simulations. This tool can therefore provide sufficient accuracy for predicting muon fluxes and angular acceptance at ground level, forming the natural entry point to the detector modeling workflow.

#### CORSIKA 8 (Full Air-Shower Modeling)

Where detailed studies of cascade development, site altitude, or overburden effects are required, the CORSIKA 8 framework offers a full Monte Carlo treatment of primary cosmic-ray air showers. Its modular framework allows interchangeable hadronic interaction models and integration with modern high-performance computing resources [32].

While excessive for routine ground-level detector design, CORSIKA 8 becomes valuable for propagating model uncertainties through to surface fluxes or for benchmarking simplified source generators such as CRY.

### 2.4.2 Transport Through Matter and Detector Response

#### Geant4

Geant4 is a C++ based Monte Carlo toolkit developed by CERN, and remains the principal toolkit used in many particle interaction studies for simulating particle transport and detector response in high-energy and astroparticle physics [33, 34]. Its physics models encompass electromagnetic, hadronic, and optical processes, enabling comprehensive

## 2.4. SOFTWARE AND SIMULATION TOOLS FOR MODELING COSMIC-RAY INTERACTIONS

modeling of muon interactions, scintillation photon generation, and light transport within one singular toolkit.

Geant4 can therefore serve as the primary simulation engine linking physical interactions to measurable observables. It allows exploration of threshold behavior, light-collection efficiency, timing resolution, and coincidence statistics under realistic geometrical configurations.

### FLUKA

FLUKA complements Geant4 as an independent transport and interaction toolkit, emphasizing high-fidelity hadronic and nuclear modeling [35]. It excels in characterizing mixed radiation fields and secondary neutron production, making it particularly valuable for cross-verification of non-muon background rates.

Using both Geant4 and FLUKA for selective benchmark cases can establish bounds on systematic uncertainty, especially in environments with significant noise, shielding or structural material around a detector.

### 2.4.3 Optical-Photon Simulation in Geant4

Simulating the full scintillation process requires detailed optical modeling. Geant4 supports this through its Optical Photon processes, enabling accurate reconstruction of light production, transport, and detection statistics [33].

The refractive index  $n(\lambda)$ , absorption and scattering lengths, and scintillation yield and decay constants must be defined for each material being simulated, which Geant4 supports [33]. These parameters govern photon propagation efficiency and temporal response. For most scintillators, published data on light yield, attenuation length, and Birks' quenching constants ensure that realistic photon budgets can be modeled in this engine [11, 10].

Accurate treatment of boundary conditions is essential in developing accurate detector simulations. Surface roughness, wrapping reflectivity, and sensor quantum efficiency must be specified to model light collection uniformity, all of which can be achieved using Geant4 Optical Surface and Logical Border Surface processes [33].

A lightweight yet rigorous simulation framework anchored by CRY and/or Geant4 can

therefore provide the analytical backbone for the design of a small-scale muon detector. Such a workflow not only supports engineering decisions but also serves as a bridge between theoretical particle physics, computational modeling, and experimental validation.

## 2.5 Related Open Designs: CosmicWatch and CosmicPi

A small number of open-source cosmic-ray detectors have emerged as valuable educational and research projects, demonstrating that compact, low-cost muon counters can achieve scientifically credible performance. Among these, *CosmicWatch* and *CosmicPi* represent two influential reference designs that inform both the technical feasibility and the design philosophy of such a project.

### 2.5.1 CosmicWatch

The CosmicWatch Desktop Muon Detector exemplifies the potential of small-scale scintillator and SiPM systems for real-time muon counting and basic data analysis [15, 36]. Its design integrates a thin EJ-200 plastic scintillator tile, a single SiPM, and a microcontroller-based readout board, all powered via USB. The documentation provides assembly instructions, calibration procedures, and open-source analysis software, making it accessible to undergraduate laboratories and outreach programs.

From a technical perspective, CosmicWatch validates key design assumptions established in this review: that minimum-ionizing muons produce reproducible photon emission pulses in scintillators, that coincidence logic suppresses environmental backgrounds, and that compact and low-voltage electronics can maintain stable operation under ambient conditions. Rate and environmental modulation results reported by the project are consistent with reference flux models discussed earlier. This confirms the reliability of its underlying physical principles, but these flux estimations were only achievable due to the project's large open-source, mass-networked operation of numerous detectors over many years [15].



### 2.5.2 CosmicPi

The CosmicPi project extends the open-source ethos to an even more networked, data-centric paradigm. It integrates plastic scintillators, SiPM readout, and GPS time synchronization on a Raspberry Pi platform [37, 38]. Its design emphasizes scalability and data sharing, enabling distributed cosmic-ray monitoring networks. The addition of GPS and environmental sensors illustrates the feasibility of time-correlated studies and geospatial data collection using affordable components.

Although much less extensively peer-reviewed than CosmicWatch, the project documentation and online blog reports successful and stable long-term operation [38]. Nevertheless, CosmicPi’s system-level design demonstrates that open muon detectors can evolve from educational tools into distributed scientific instruments.

## 2.6 Conclusion of Literature Review

The reviewed literature collectively establishes a coherent foundation for the design of a compact desktop muon detector. Each area of research, from cosmic-ray physics to detector materials, photodetector technologies, and simulation frameworks, converges on a consistent set of design principles that inform both the physical configuration and operational strategy of this project.

First, the study of cosmic radiation and secondary muon flux confirms that the surface muon environment is well understood and sufficiently intense for small-scale detection. Empirical flux models and atmospheric parameterizations demonstrate that statistically meaningful data can be obtained with an active area on the order of tens of square centimetres (assuming coincidence detection). The consistency of these models with experimental benchmarks gives confidence that a compact, two-layer telescope geometry will yield reliable muon rate measurements.

Second, the comparative evaluation of detection mechanisms identifies plastic scintillation as the most balanced and practical approach for this scale of instrumentation. Its rapid response, relatively low price-point, near-linear light yield in the minimum-ionizing regime, and mechanical stability ensure accurate and reproducible signal generation. Alternative technologies such as liquid scintillators, Cherenkov cells, or gaseous detectors either impose excessive complexity, cost, or fail to improve sensitivity in this flux regime.

## 2.6. CONCLUSION OF LITERATURE REVIEW

Third, the comparison between SiPMs and PMTs clearly supports the use of SiPMs for this application. Their compactness, low-voltage operation, and direct circuit integration align with the project's aims of portability, modularity, and accessibility, while their timing precision and gain stability remain sufficient for coincidence-based muon detection. When operated in coincidence, their higher dark-count rate becomes negligible, confirming their suitability for low-rate cosmic-ray measurements.

Simulation frameworks such as Geant4 further reinforce these design choices by providing a validated link between theoretical flux models, detector geometry, and experimental observables. This integration of modeling with design ensures that calibration is not an afterthought but a natural verification of physically grounded expectations.

Finally, examination of open-source detector initiatives such as *CosmicWatch* and *CosmicPi* demonstrates the feasibility and educational value of this approach. These precedents confirm that accessible, low-cost coincidence muon detectors can achieve scientific credibility when underpinned by robust calibration, transparent documentation, and reproducible physics.

In synthesis, the literature points decisively toward a detector architecture comprising:

1. At least 2 stacked plastic scintillator tiles, optimized for coincidence-based muon detection;
2. Silicon photomultiplier (SiPM) readout, providing compact, low-power optical conversion;
3. A Geant4 simulation workflow, ensuring predictive calibration and design validation; and
4. Reproducible, structured data logging, enabling transparent data acquisition and potential networked expansion with multiple detectors.

This architecture emerges not as an arbitrary choice but as the logical conclusion of current evidence, research, and practices in compact cosmic-ray detection. It establishes a robust foundation for the subsequent design, calibration, and testing phases of this study.

# Chapter 3

## Design Methodology and Theoretical Framework

### 3.1 Overview of Methodological Approach

The overall methodological framework of this project evolved directly from the research and practical constraints identified during its early development. Established in section 2.1 and section 2.2, cosmic-ray muons represent an ideal subject for small-scale experimental study due to their high flux at sea level and well-characterized energy spectrum. However, as discussed in section 2.5, even well-documented open-source projects such as *CosmicWatch* and *CosmicPi* operate at the limits of what is achievable for singular compact detectors, and rely on coincidence measurements or large-scale distributed networks to obtain statistically significant flux data.

Within this context, the realities of a 12-week project timeline and a strict budget cap of R2000 imposed significant limitations on both component access and experimental validation. Procuring a suitable plastic scintillator proved especially challenging: available options were either prohibitively expensive or subject to international shipping delays exceeding the entire project duration. Only by week six was access secured to a single  $25\text{ cm} \times 1\text{ cm} \times 1\text{ cm}$  EJ-200 scintillator rod, generously loaned by UCT’s muon laboratory. Because the scintillator’s geometry and optical characteristics directly inform all aspects of detector design, major portions of the project’s design and component procurement could not commence until this material was confirmed.

Budgetary restrictions further ruled out multi-layer coincidence detection, reducing the

detector to a single scintillator–SiPM channel. Without coincidence or calibrated shielding, true muon event discrimination and muon flux measurement was not experimentally attainable within the available resources. Combined with limited fabrication time for a custom SiPM PCB, these factors rendered a fully empirical approach infeasible.

Consequently, the project adopted a **simulation-centered design methodology** that emphasizes theoretical validation, controlled simulation studies, and partial hardware prototyping. Although real-time flux measurement was beyond scope, a complete and validated detection pipeline from particle-level interaction to data acquisition could still be demonstrated.

#### 3.1.1 Revised Research and Design Workflow

In response to constraints, the detector was restructured into three interdependent subsystems, each addressing a key stage of the detection process:

1. **Scintillator Simulation Subsystem:** A detailed `Geant4` simulation that models muon energy deposition, photon generation, and transport within the EJ-200 scintillator.
2. **Analog Front-End (AFE) Subsystem:** A transimpedance amplifier and peak detector circuit which converts simulated or injected SiPM currents into measurable voltage pulses, verified through `LTSpice` simulation and bench testing.
3. **Data Logging and Firmware Subsystem:** An `Arduino Nano` and `Python`-based logging interface capture and timestamp detector signals, with environmental data included for future correlation studies.

These three subsystems form an integrated workflow linking simulation, circuit design, and data acquisition. Simulated photon yields from the first subsystem are translated into equivalent SiPM charge and current profiles, which serve as inputs for circuit testing in the second subsystem, which then interfaces with the final subsystem. This simulation-centric design ensured that each subsystem was individually verifiable, analytically consistent, and extensible for future hardware integration.

### 3.1.2 Revised Project Goals and Scope

The limitations imposed by time, budget, and component availability necessitated refinement of the original aims outlined in chapter 1. Table 3.1 below summarizes how the project objectives evolved in response to these constraints.

Table 3.1: Comparison of original and revised project goals and scope.

Original Project Goals	Revised Goals and Scope
Design and construct a fully operational desktop muon detector capable of recording real muon events and estimating flux.	Develop a simulation-validated detector framework demonstrating the full detection and signal-processing chain, without requiring empirical flux measurement.
Perform experimental validation using scintillator–SiPM coincidence detection.	Conduct Geant4-based simulations of muon–scintillator interactions and verify analog circuit performance via current-injection testing.
Implement real-time data logging and environmental correlation with measured muon flux.	Develop a modular Python-based data logging program capable of timestamping simulated or test-pulse data, incorporating environmental parameters for future integration.
Complete PCB fabrication and full hardware assembly of a functional prototype.	Partially fabricate and test the analog readout circuit using discrete components; integrate simulation and hardware data to validate design feasibility.

These refined objectives establish the structure for the remainder of this design methodology chapter.

## 3.2 Geant4 Scintillator Simulation Subsystem Design

The detector simulation implemented in this project is the first subsystem of the overall design workflow. It translates the physical models of muon interaction, scintillation, and photon detection (as informed by the literature explored in subsection 2.1.3 and section 2.3) into a computational framework using the **Geant4** simulation toolkit.

### 3.2.1 Overview of the Geant4 Simulation Framework

**Geant4** is a C++ based Monte Carlo toolkit developed by CERN for simulating the passage of particles through matter (see subsection 2.4.3). The **Geant4** simulation is organized around an object-oriented class hierarchy composed of interdependent classes that define distinct components of the simulated detector and its interactions:

- **DetectorConstruction.cc:** Defines the geometry, materials, and optical surfaces of the detector. Specifies the EJ-200 scintillator, SiPM window, reflective wrapping, and optical coupling layers.
- **Physics Package:** Specifies the physical processes and particle types to be simulated. Utilizes the predefined **Geant4 QGSP\_BERT** C++ class, which incorporates electromagnetic and hadronic interactions relevant to cosmic-ray muons.
- **PrimaryGeneratorAction.cc:** Defines the characteristics of the incoming primary particle source: muons with configurable energy, trajectory, and angular distributions.
- **RunAction.cc, EventAction.cc, and SteppingAction.cc:** Controls the execution flow of the simulation at different levels of granularity. **RunAction** initializes data structures for each simulation run, **EventAction** handles per-event CSV data recording such as photon counts and energy deposition, and **SteppingAction** monitors the physical steps taken by each particle through the geometry.
- **StackingAction.cc:** Manages the priority of particle tracks, ensuring that optical photons generated by scintillation are appropriately tracked after the primary muon interactions within the scintillator.

Figure 3.1 outlines the class structures and data dependencies that constitute the working simulation.

The full source code for this simulation (and all other subsequent code files designed in this chapter) can be found in the project GitHub repository available in the appendix.

### 3.2.2 Simulation Workflow and Event Handling

The simulation proceeds through the hierarchical execution cycle controlled by the **Geant4** kernel:

### 3.2. GEANT4 SCINTILLATOR SIMULATION SUBSYSTEM DESIGN

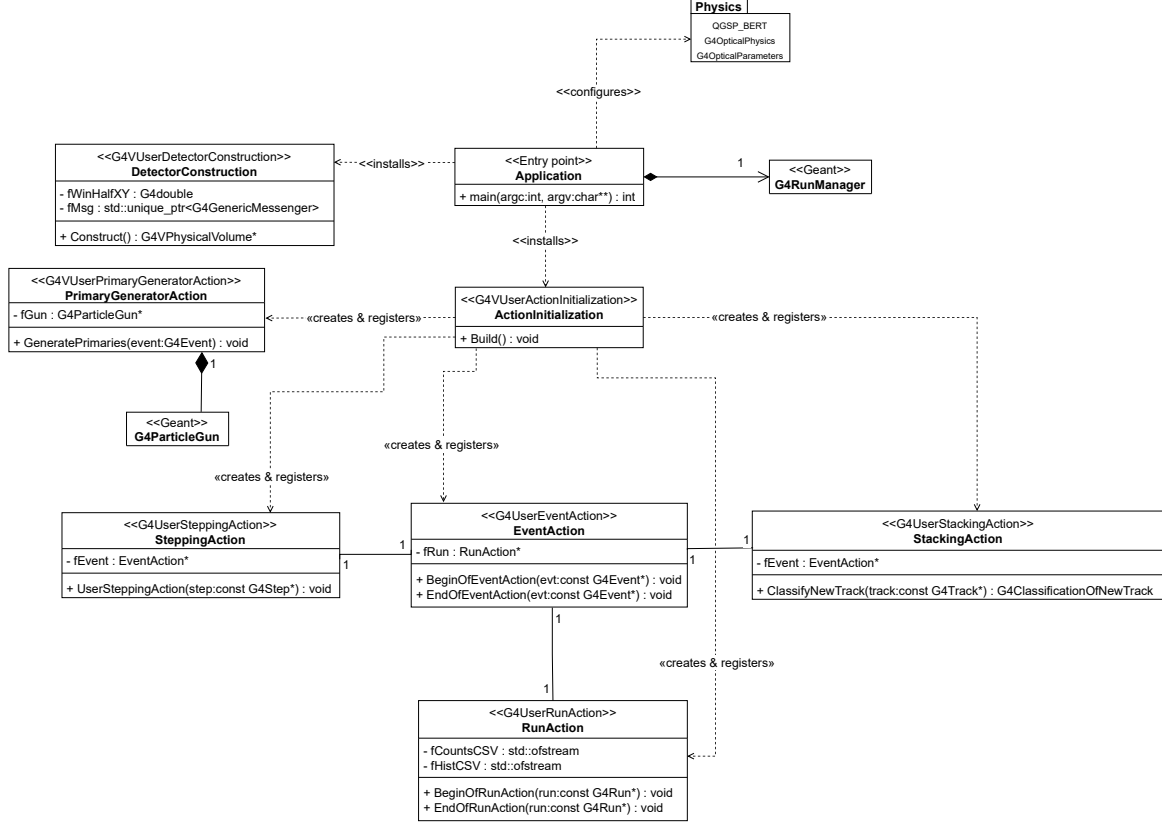


Figure 3.1: Simplified UML class diagram of the Geant4 simulation.

1. The primary generator emits a muon with variable energy levels and directions, which then enters the scintillator volume.
2. The tracking manager propagates the muon through the material, invoking the physics list to compute energy loss, ionization, and photon production at each step.
3. Each scintillation photon is treated as an individual optical particle, transported according to boundary and optical properties defined in the **DetectorConstruction** class.
4. The event manager compiles all photons detected at the SiPM surface during a single muon event, writing them to output CSV files via **EventAction**.

This hierarchical process allows fine-grained control of both physical and statistical behavior. The modular class design also enables later reconfiguration such as substituting a different scintillator or SiPM material definition without altering the overall simulation logic.

### 3.2.3 Physics Model Selection and Energy Deposition

Muon transport and energy loss were simulated using the `QGSP_BERT` physics list with electromagnetic processes enabled. This combination captures the dominant interaction mechanisms relevant to minimum-ionizing muons while maintaining computational efficiency. The mean energy loss per unit path length ( $dE/dx$ ) is automatically evaluated according to the Bethe-Bloch formula discussed in subsection 2.1.3, ensuring consistency between real-world and simulated energy deposition.

To model nonlinear light yield at higher ionization densities, the simulation explicitly includes Birks' quenching in `DetectorConstruction` via:

```
EJ200->GetIonisation()->SetBirksConstant(0.156*mm/MeV);
```

This value corresponds to typical Birks' constants reported for polyvinyltoluene-based EJ-200 scintillators (see section 2.1.3) [10] and ensures that simulated photon yields remain physically realistic across varying muon energies and trajectories.

### 3.2.4 Material Definitions and Scintillator Optical Properties

The EJ-200 scintillator was implemented as a custom material with C:H atomic ratio 1:1, defined through the `G4NistManager` interface. A detailed `G4MaterialPropertiesTable` specifies its optical characteristics according to the official Eljen Technology datasheet [39], including refractive index, emission spectrum, light yield, and decay constants:

```
"SCINTILLATIONYIELD", 10000/MeV
"FASTTIMECONSTANT", 2.1*ns
"RINDEX", 1.58
```

The emission band (2.0–3.5 eV) corresponds to 620–354 nm, peaking near 425 nm, which overlaps strongly with the blue-sensitive region of typical SiPMs, established in subsection 2.3.2. The decay constant neglects slower secondary Cherenkov emission components that are negligible on nanosecond timescales relevant to this study.



### 3.2.5 Geometry and Boundary Conditions

The detector geometry, defined in `DetectorConstruction.cc`, models the  $25\text{ cm} \times 1\text{ cm} \times 1\text{ cm}$  EJ-200 bar wrapped in a reflective layer similar to the aluminium foil wrapping around the actual scintillator bar used (98% reflectivity) and optically coupled to a SiPM window using a thin layer of optical gel (typical refractive index  $n = 1.46$ ). The SiPM window itself is interfaced to the only  $1\text{ cm} \times 1\text{ cm}$  face of the scintillator that is not wrapped in foil, and was modeled as  $\text{SiO}_2$  ( $n = 1.52$ ), matching the refractive index values of commonly available SiPM sensors [40, 39]. These values ensure that total internal reflection, boundary losses, and Fresnel effects are realistically captured according to the optical modeling principles discussed in subsection 2.4.3.

Photons reaching the SiPM window were assigned a constant photon detection efficiency (PDE) of 63%, representative of blue-sensitive SiPMs at moderate overvoltages [40] and sufficient to compare the performance between simulated and reported results.

### 3.2.6 Photon Detection and Event Tracking

Within the `Geant4` framework, each scintillation photon produced by muon energy deposition in the EJ-200 volume is propagated until it is either absorbed, reflected, or reaches the SiPM detection surface. Optical processes including reflection, refraction, and boundary absorption are handled through the `G4OpBoundaryProcess` class, using the material and surface properties defined in `DetectorConstruction.cc`. This allows the simulation to model realistic photon transport and collection efficiency at the scintillator–SiPM interface.

Detected photons are registered in `EventAction.cc`, where each optical photon crossing the SiPM boundary is recorded as a detection event. The total number of photons detected per muon event (and other relevant observables discussed in subsection 3.2.7) are written to a CSV output file for subsequent analysis.

The exported datasets provide a direct link between simulated particle interactions and the observable optical signal at the SiPM window. These event-level photon counts are translated through calculation into charge and current profiles specific to the SiPM used in the analog front-end subsystem.

### 3.2.7 Simulation Outputs and Observable Parameters

The simulation produces two primary CSV outputs that capture all relevant observables from each muon event:

- **photon\_counts.csv:** Contains event-wise quantities including total scintillation photons generated, photons reaching the SiPM window, and the number ultimately detected. It also includes the corresponding muon track length and total energy deposited within the scintillator volume, enabling later validation of the expected Bethe-Bloch plateau behavior across varied muon energies through testing.
- **time\_histograms.csv:** Records the temporal distribution of photon arrivals at the SiPM surface, allowing analysis of timing dispersion and decay characteristics associated with the EJ-200 scintillator’s response.

Together, these outputs form the quantitative link between particle-level interaction modeling and the subsequent circuit-level subsystem.

In addition to numerical data, a 3D interactive visualization macro using `OpenGL` was developed to render muon trajectories, scintillation photon paths, and optical boundary interactions within the `Geant4` geometry. This visualization served as both a diagnostic and interpretive tool, confirming correct implementation of material boundaries, optical properties, and detector placement, shown in Figure 3.2. Figure 3.3 shows the actual EJ-200 rod (with the same SiPM interfacing and reflective wrapping) being modeled for comparison with the simulated geometry.

### 3.2.8 Overall Subsystem Design

This simulation design can thus be used to convert the theoretical particle propagation principles established in the literature review into a reproducible, data-generating model that will be interfaced directly with the circuit-level and data-logging subsystems.

Macro-controlled simulation runs will be used to conduct systematic parameter studies under controlled conditions. This design aspect enables a scientifically rigorous evaluation of how individual factors influence scintillation light yield, photon transport, SiPM detection probability, and whether or not the results agree with real-world physics.

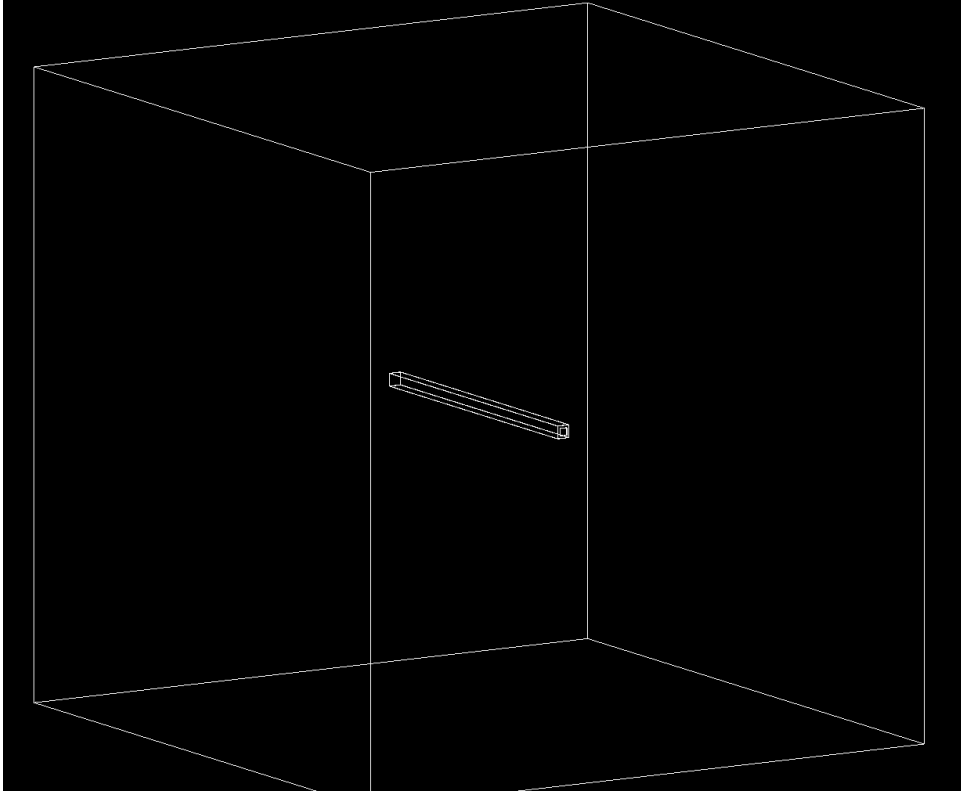


Figure 3.2: 3D interactive visualization of the simulated EJ-200 scintillator and SiPM window in `Geant4`.

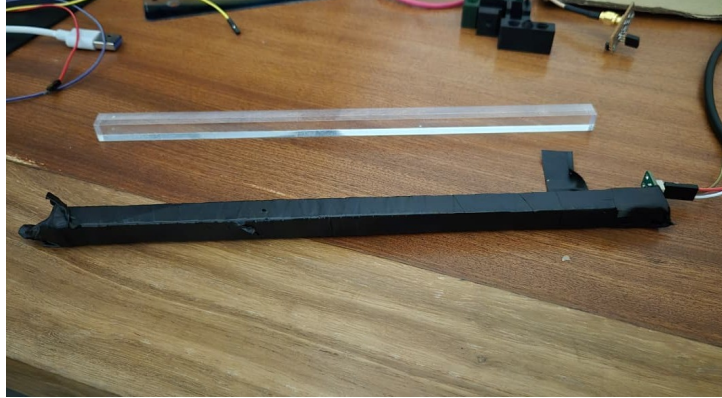


Figure 3.3: Physical EJ-200 rods from UCT's Muon Lab (with and without reflective wrapping).

## 3.3 Analog Front-End (AFE) Subsystem Design

The analog front-end (AFE) subsystem is responsible for converting the current pulses produced by the SiPM into measurable voltage signals suitable for digitization and logging with the portable desktop-based logging subsystem. Its design must be based on established principles for SiPM readout circuits and aim to balance sensitivity, bandwidth, and simplicity within the project's resource constraints.

### 3.3. ANALOG FRONT-END (AFE) SUBSYSTEM DESIGN

The subsystem comprises three cascaded stages:

1. A **transimpedance amplifier (TIA)** that converts the SiPM’s fast, low-amplitude current pulses into voltage signals.
2. A **peak detection and hold circuit** that captures and holds the maximum voltage of the TIA output corresponding to each SiPM pulse.
3. An **RC low-pass filter** that smooths the held voltage for ADC conversion.

Each stage was designed based on analytical performance targets derived from SiPM operating characteristics and literature-reported circuit architectures.

#### 3.3.1 Literature-Informed Circuit Design

SiPMs produce short current pulses (10–100 ns) with amplitudes of tens to hundreds of microamperes dependent on photon yield [40]. To measure these signals effectively, the front-end must: (1) convert fast current pulses into measurable voltages, (2) extend their duration for sampling by slower microcontrollers, and (3) filter and condition the output for noise-free ADC detection.

Through literature review, the TIA emerged as a standard front-end topology for SiPMs [30], providing linear current-to-voltage conversion while mitigating effects of junction capacitance. Because the resulting voltage pulses remain shorter than typical ADC sampling intervals ( $< 10 \mu\text{s}$ ), a peak-hold circuit is introduced to capture and maintain the pulse’s maximum amplitude. The final RC low-pass filter then suppresses high-frequency and sampling noise, yielding a stable voltage signal suitable for digitization. These principles, widely demonstrated in cosmic-ray and scintillation detector literature, helped form the basis of this project’s AFE architecture. The *CosmicWatch* project employs roughly the same analogue signal-shaping structure of a TIA stage and op-amp trigger, further validating these design choices [21].

#### 3.3.2 Derived AFE Performance Requirements

Circuit performance requirements were established from an SiPM’s expected signal profile and the inherent desktop-based system constraints [30, 40]. Table 3.2 summarizes these design targets.

### 3.3. ANALOG FRONT-END (AFE) SUBSYSTEM DESIGN

Table 3.2: Derived performance targets for the AFE subsystem.

Parameter	Design Rationale	Target
Bandwidth ( $f_{-3\text{dB}}$ )	Must capture SiPM pulses of 20–100 ns duration.	$> 20$ MHz
Transimpedance Gain ( $R_f$ )	Convert $\mu\text{A}$ SiPM pulses to ADC-detectable voltage swings.	200–500 $\Omega$
Input-Referred Noise	Maintain $SNR > 20$ dB for minimum photon event.	$< 5$ nV/ $\sqrt{\text{Hz}}$
Hold Time Constant ( $\tau_h = R_2C_3$ )	ADC sampling window (10-bit, $< 10$ kHz) requires ms-scale decay.	1–3 ms
Output Filter Cutoff ( $f_c$ )	Suppress noise while preserving pulse envelope.	50–100 Hz
Supply Voltage	Compatibility with portable/USB-based voltage supply.	+5 V single rail

These specifications form the basis for component selection and deriving passive element values.

#### 3.3.3 Component Evaluation and Selection

Each key component was selected based on the circuit performance requirements in Table 3.2, balanced against cost, practicality, local availability, and delivery lead times.

#### SiPM Device Evaluation

The Broadcom AFBR-S4N66P014M device was chosen due to its high photon detection efficiency (PDE = 63% at 425 nm) and moderate terminal capacitance ( $\sim 100$  pF). The active window size of this specific SiPM is 6mm $\times$ 6mm, while other SiPMs at similar price points have smaller active window sizes. The AFBR-S4N66P014M was also one of the very few SiPMs that had a tolerable delivery lead time. Alternative options considered are shown in Table 3.3, all of which was required to have a peak wavelength of 420–425nm to match the EJ-200 emission spectrum [40, 41, 42].

### 3.3. ANALOG FRONT-END (AFE) SUBSYSTEM DESIGN

Table 3.3: Comparison of candidate SiPM devices.

Device	PDE (%)	Window Size	Capacitance (pF)	Recovery (ns)	Notes
Broadcom AFBR-S4N66P014M	63	6mmx6mm	100	55	Selected; available at UCT stock.
Hamamatsu S13360-1350CS	40	1.3mmx1.3mm	120	70	Smaller window, longer recovery.
MicroFC-60035-SMT	31	3mmx3mm	150	65	Low PDE, unavailable locally.

#### TIA Operational Amplifier Selection

For the TIA, the operational amplifier required a high gain-bandwidth product (GBP), low input capacitance, and minimal noise to maintain stability with the SiPM's capacitance. Table 3.4 summarizes candidate devices [43, 44, 45].

Table 3.4: Comparison of candidate op-amps for the TIA stage.

Device	GBP (MHz)	Input Cap (pF)	Noise ( $\text{nV}/\sqrt{\text{Hz}}$ )	Input Bias (pA)	Remarks
OPA656	230	2.6	6.0	2	Stable, good balance of speed/noise.
OPA657	1600	4.5	4.8	2	Excessive GBP, stability risk.
AD8065	145	6.6	7.0	1	Bandwidth borderline for 20 ns pulses.

The OPA656 was selected to provide adequate bandwidth under a 5 V supply, with stable phase margin, fast slew rate, and acceptable noise performance. This op-amp is commonly used for photodetector transimpedance amplification according to its datasheet, further supporting its suitability for this application.

#### Peak Detector Operational Amplifier and Diode Selection

The performance of the peak-detection stage depends primarily on the operational amplifier's slew rate, input bias current, and output swing, as these parameters dictate how accurately

### 3.3. ANALOG FRONT-END (AFE) SUBSYSTEM DESIGN

fast voltage peaks from the TIA are captured and transferred to the RC hold network. A single-supply, rail-to-rail op-amp with low noise and sufficient gain-bandwidth product (GBP) was therefore required. Table 3.5 summarizes the candidate devices considered for this stage [46, 47, 48].

Table 3.5: Comparison of operational amplifiers evaluated for the peak-detection stage.

Device	GBP (MHz)	Slew Rate (V/ $\mu$ s)	Input Bias (pA)	Supply Range (V)	Remarks
OPA365	50	25	0.2	2.2–5.5	Fast, low noise, ideal for single-supply operation.
OPA350	38	22	0.5	2.5–5.5	Similar speed, not locally available.
MCP6022	10	7	1	2.5–6.0	Cheaper, but insufficient GBP for ns pulses.

The OPA365 was chosen for its superior combination of bandwidth, fast slew rate, and rail-to-rail I/O capability under a single 5 V supply. Its input bias current of only 0.2 pA ensures minimal discharge of the hold capacitor, maintaining accurate voltage retention during the decay period. This device therefore offers a stable and precise solution for tracking transient peaks from the SiPM pulse while remaining compatible with low-voltage system constraints.

Although the diode choice is less critical, a small-signal Schottky diode (BAT85) was incorporated into this stage for its low forward voltage and fast recovery, ensuring minimal charge loss at the op-amp input.

#### 3.3.4 Analytical Derivation of Passive Component Values

The passive component values for the analog front-end were derived from the design targets established in subsection 3.3.2 using first-principle calculations. Each stage was dimensioned to ensure that the system bandwidth, gain, and timing characteristics satisfied both the SiPM signal dynamics and the ADC sampling limitations.

#### Transimpedance Amplifier Design

The TIA converts the SiPM's current pulses into corresponding voltage signals according to:

$$V_{\text{out}}(t) = -R_f i_{\text{SiPM}}(t), \quad (3.1)$$

where  $R_f$  is the feedback resistor and  $i_{\text{SiPM}}(t)$  represents the SiPM current pulse. The feedback resistor determines the transimpedance gain, while a parallel feedback capacitor  $C_f$  sets the amplifier bandwidth and stabilizes the circuit against the SiPM's junction capacitance.

To accurately reproduce pulse widths on the order of tens of nanoseconds, the  $-3$  dB frequency must exceed 20 MHz. For a single-pole approximation, the bandwidth of the TIA can be expressed as:

$$f_{-3\text{dB}} = \frac{1}{2\pi R_f C_f}. \quad (3.2)$$

Substituting a target cutoff of  $f_{-3\text{dB}} = 110$  MHz ( $>5\times$  the initial target to preserve signal fidelity without distortion), the relationship between  $R_f$  and  $C_f$  becomes:

$$R_f = \frac{1}{2\pi f_{-3\text{dB}} C_f}. \quad (3.3)$$

Choosing a practical feedback capacitance of  $C_f = 3.0$  pF (consistent with the OPA656 input compensation range) yields:

$$R_f = \frac{1}{2\pi(110 \times 10^6)(3.0 \times 10^{-12})} \approx 480 \, \Omega. \quad (3.4)$$

A standard  $470 \, \Omega$  resistor was selected as the nearest E24 value, providing a transimpedance gain of approximately  $0.47$  V/mA (according to Equation 3.1) while maintaining phase stability. This bandwidth comfortably accommodates SiPM current pulses as short as 20 ns.

#### Peak-Hold Circuit Design

The hold time-constant of this stage is governed by the resistor-capacitor network connected to the op-amp output:

$$\tau_h = R_2 C_3, \quad (3.5)$$



### 3.3. ANALOG FRONT-END (AFE) SUBSYSTEM DESIGN

where  $\tau_h$  determines the exponential decay rate of the stored voltage according to:

$$V_{C_3}(t) = V_p e^{-t/\tau_h}. \quad (3.6)$$

To ensure compatibility with most cheap microcontroller ADC's (sampling below 10 kS/s), the voltage should remain held for at least 1 ms. Setting a target hold time constant of  $\tau_h = 1.2$  ms ensures a slow enough decay for reliable sampling without introducing excessive overlap between events. Using a practical resistance of  $R_5 = 5.6$  k $\Omega$ , the required capacitance is:

$$C_6 = \frac{\tau_h}{R_5} = \frac{1.2 \times 10^{-3}}{5.6 \times 10^3} \approx 220 \text{ nF}. \quad (3.7)$$

This capacitance provides a smooth exponential discharge characteristic suitable for the event rate expected in single-channel muon detection.

#### Output Low-Pass Filter Design

To reduce high-frequency noise from both the TIA output and ADC quantization, a simple first-order RC low-pass filter was included after the peak-hold stage. The cutoff frequency of this filter is given by:

$$f_c = \frac{1}{2\pi R_1 C_2}. \quad (3.8)$$

The cutoff frequency was chosen to be 2 kHz to ensure stable digital readings while maintaining event distinguishability. With a target of  $f_c = 2$  kHz, a resistance of  $R_1 = 1$  k $\Omega$  leads to:

$$C_2 = \frac{1}{2\pi R_1 f_c} = \frac{1}{2\pi(1000)(2000)} \approx 100 \text{ nF}. \quad (3.9)$$

This configuration filters noise above approximately 2 kHz, improving the readability of held voltages without significantly delaying reset between successive pulses.

### 3.3. ANALOG FRONT-END (AFE) SUBSYSTEM DESIGN

#### Design Verification Summary

The final component values derived analytically were:

$$\begin{aligned} R_f &= 470 \, \Omega, & C_f &= 3.0 \, \text{pF}, \\ R_2 &= 5.6 \, \text{k}\Omega, & C_3 &= 220 \, \text{nF}, \\ R_1 &= 1 \, \text{k}\Omega, & C_2 &= 100 \, \text{nF}. \end{aligned}$$

These satisfy the required bandwidth, hold-time, and cutoff specifications summarized in Table 3.2. All component values will be verified in LTSpice simulations to confirm stability and transient performance under injected current pulse excitation and will be discussed in chapter 4.

#### Final Circuit Design

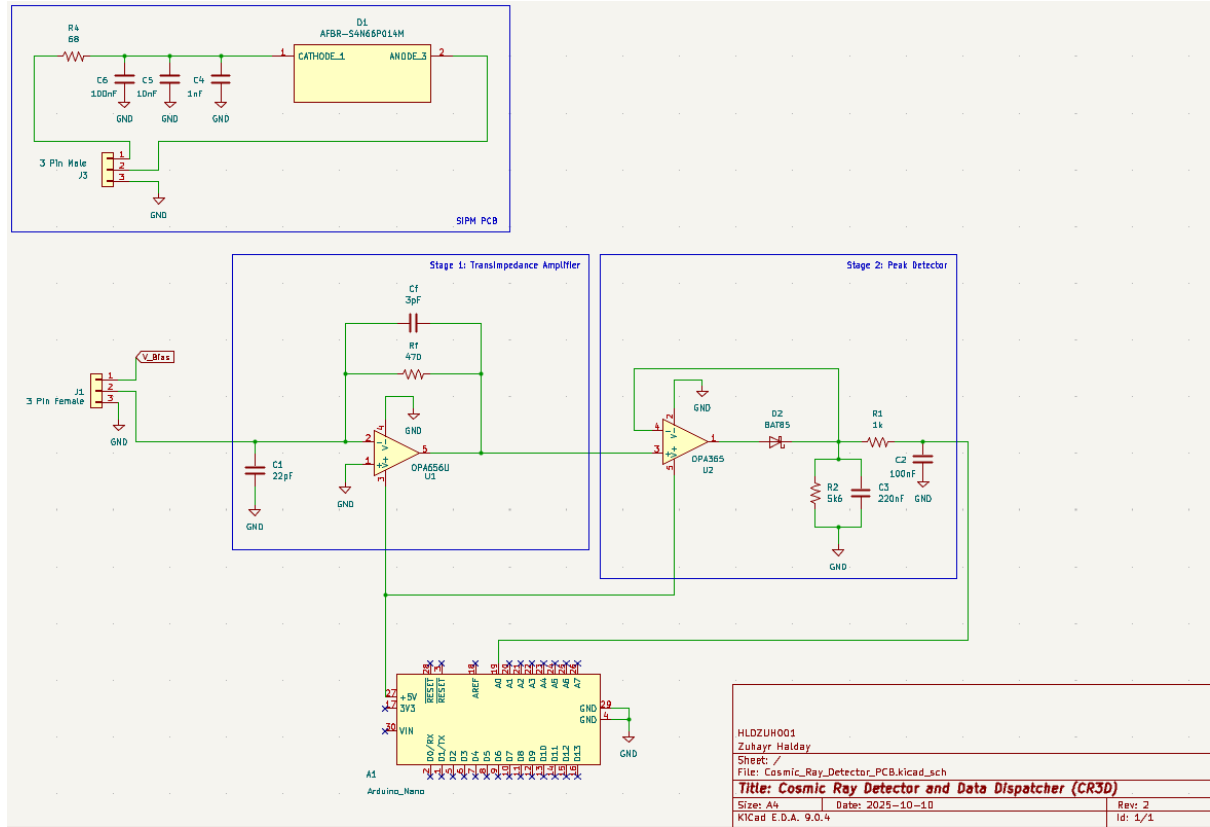


Figure 3.4: KiCAD Schematic of the final AFE circuit.

#### 3.3.5 Hardware Implementation and Experimental Constraints

Following the analytical design phase, the AFE circuit was assembled on a prototyping Veroboard to minimize cost and avoid delays associated with outsourced PCB fabrication. However, the surface-mounted SiPM required shorter interconnects and controlled impedance, necessitating the fabrication of a custom printed circuit board (PCB). A DIY etching process was therefore employed to meet these constraints within the project timeline and budget.

The PCB was designed in KiCAD with 0.4mm track widths and printed onto thermal transfer paper using a laser printer. Tracks were transferred onto a copper-clad board via heat pressing, followed by chemical etching in ferric chloride to remove unmasked copper. Through-hole vias were manually hand-drilled, and components were manually soldered onto the etched board. This toner-transfer and ferric-chloride process achieved fine trace resolution and enabled rapid prototyping of a custom PCB at minimal cost.



Figure 3.5: Toner transfer and ferric chloride PCB etching process.

The Broadcom AFBR-S4N66P014M SiPM was subsequently surface-mounted using a soldering iron. However, the process resulted in an internal short between the anode and cathode pads beneath the SiPM window, rendering the sensor inoperable. This soldering process is typically performed using a hot-air reflow station, but such equipment was not accessible within the project's condensed timeframe. Due to its unique pad geometry and the absence of a replacement within the available budget and timeframe, optical

### 3.3. ANALOG FRONT-END (AFE) SUBSYSTEM DESIGN

testing with the EJ-200 scintillator bar could not proceed. In response, circuit validation was conducted via current-injection testing, replicating the expected SiPM current pulse using an RC pulse network based on the scintillator simulation subsystem's results.

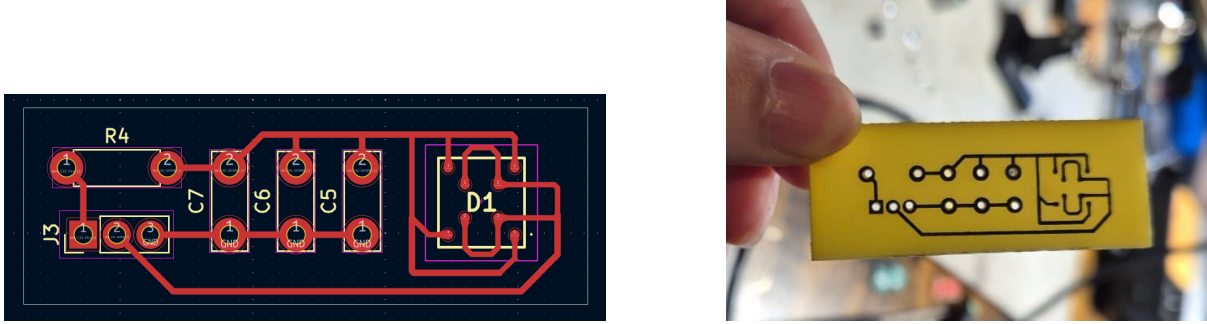


Figure 3.6: KiCAD SiPM PCB Design (left) in comparison to final etched PCB (right).

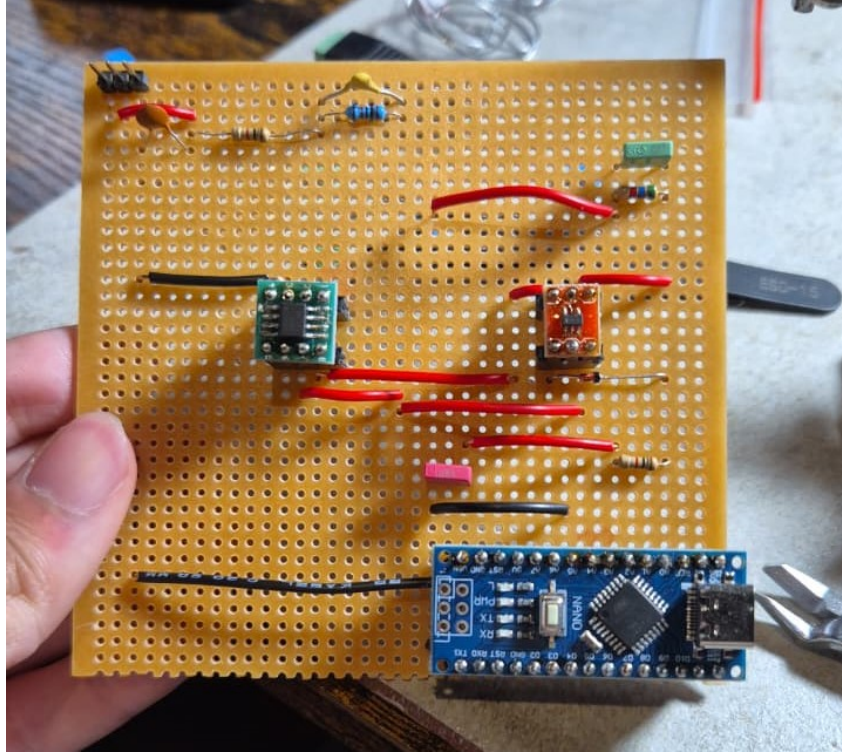


Figure 3.7: Final hardware-prototyped AFE circuit.

#### 3.3.6 Acceptance Testing Matrix

An acceptance test matrix was established to quantify subsystem performance against the requirements in Table 3.2. This is a very brief testing matrix due to the AFE's relatively straightforward design. Each test will be revisited in chapter 4 for validation through simulation and bench measurements.

### 3.4. FIRMWARE AND DATA-LOGGING SUBSYSTEM DESIGN

Table 3.6: Acceptance test matrix for AFE subsystem.

ID	Stage	Expected Behaviour	Target Metric	Verification Method
AFE-1	TIA	Stable baseline noise at zero input current.	$V_{\text{RMS noise}} < 10 \text{ mV}$	Oscilloscope test
AFE-2	Peak Hold	Holds voltage for set decay constant.	$\tau_h = 1.2 \pm 0.1 \text{ ms}$	Pulse injection test
AFE-3	Full Chain	Output voltage proportional to injected charge.	Output gain $\approx 0.47 \text{ V/mA}$	Bench test and simulation agreement
AFE-4	Full Chain	Entire AFE subsystem performs reliably on single 5V supply	No output clipping or saturation at 5 V supply	Bench/Oscilloscope testing

#### 3.3.7 Overall Subsystem Design

The AFE subsystem was designed using literature-informed analogue circuit design principles and quantitative analysis to ensure that each signal-shaping stage met its derived performance requirements. Component choices were justified through calculations, comparison against electrical performance, practical considerations, and cost constraints. Although full optical testing was impeded by hardware failure, simulation modeling and current-injection testing can confirm whether the circuit operates within expected limits, providing a validated foundation for integration with the data logging subsystem.

## 3.4 Firmware and Data-Logging Subsystem Design

The firmware and data-logging subsystem establishes the digital acquisition and visualization link between the analog front-end (AFE) and a host computer. Its role is to convert analog voltages into structured, timestamped data while providing real-time visual and statistical feedback during operation. Although the programming implementation is relatively standard, its design philosophy is rooted in ensuring reproducibility, data integrity, and temporal synchronization. This subsystem therefore bridges the transition between the analog and digital domains, ensuring that physical detector behavior can be accurately observed, recorded, and analyzed.

### 3.4.1 Design Objectives and Role within the System

The subsystem was designed to achieve the following objectives:

- Digitize and transmit AFE output signals for software-level event processing.
- Provide a graphical interface for live monitoring and logging of detector activity.
- Record structured, timestamped data suitable for data analysis and correlation.
- Maintain timing consistency between hardware (microcontroller) and software clocks.

Together, these features establish a complete acquisition pipeline from detector output to persistent and interpretable data.

### 3.4.2 Microcontroller Selection and Justification

The only physical component requiring design justification in this subsystem is the data acquisition microcontroller. Candidate devices were compared based on analog-to-digital conversion (ADC) precision, communication interface, voltage compatibility, and firmware development simplicity. Table 3.7 summarizes this comparison.

Table 3.7: Comparison of candidate microcontrollers for data acquisition.

Device	ADC Res.	Max Sample Rate	Supply (V)	Interface	Remarks
Arduino Nano (ATmega328P)	10-bit	9.6 kS/s	5.0	USB/Serial	Selected: simple, 5 V compatible, widely supported.
ESP32	12-bit	100 kS/s	3.3	USB/Wi-Fi	Higher performance, but requires 3.3 V redesign.
STM32F103	12-bit	1 MS/s	3.3	USB/Serial	Complex firmware and driver dependencies.

The Arduino Nano was selected for its cheap price point, reliability, compatibility with the single 5 V system rail, and its integrated serial–USB interface, allowing seamless communication with Python on the host computer. Its 10-bit ADC precision and 9.6 kS/s effective sampling rate are sufficient for the AFE’s peak-hold output, which changes on millisecond timescales. This choice minimizes system complexity and cost while ensuring

reliable, synchronized data capture. Its use in the *Cosmic Watch* project verifies that it is a viable choice for this application [21].

### 3.4.3 Firmware Design

The firmware, implemented in C++ using the Arduino IDE, performs continuous analog sampling, event discrimination, and structured serial data transmission to the host computer. Its control logic is intentionally minimalist to preserve timing and minimize computational overhead, while higher-level data handling and analysis are delegated to the host-side software. In addition to its acquisition role, the firmware also configures a 5 V digital pulser on one of the Arduino's output pins, enabling self-contained testing of the AFE subsystem. When routed through a simple RC low-pass network, this pulser produces a shaped voltage waveform that can be applied to the AFE input, effectively emulating SiPM current pulses. The inclusion of a configurable pulser can thus facilitate functional verification of the AFE, allowing validation that variations in the input excitation produce corresponding and measurable changes at the circuit output. A simplified flow diagram of the firmware's logical operation is shown in Figure 3.8.

#### Core operation:

1. The program initializes serial communication at 115200 baud and configures the A2 ADC input pin connected to the AFE output.
2. During each loop iteration, it reads the analog voltage, subtracts a fixed baseline, and compares the result to a configurable threshold.
3. If the threshold is exceeded, the voltage is recorded as a detected event, and the microsecond counter is used to determine the dead time since the previous event.
4. The resulting data is serialized into JSON-formatted strings and transmitted to the host computer for parsing and storage.

Each message is structured to distinguish ordinary samples from valid events:

```
{"type": "sample", "mv": 812.3, "adc": 166}
{"type": "event", "mv_peak": 1035.4, "adc_peak": 212, "baseline_adc": 166, "dead_us": 90}
```

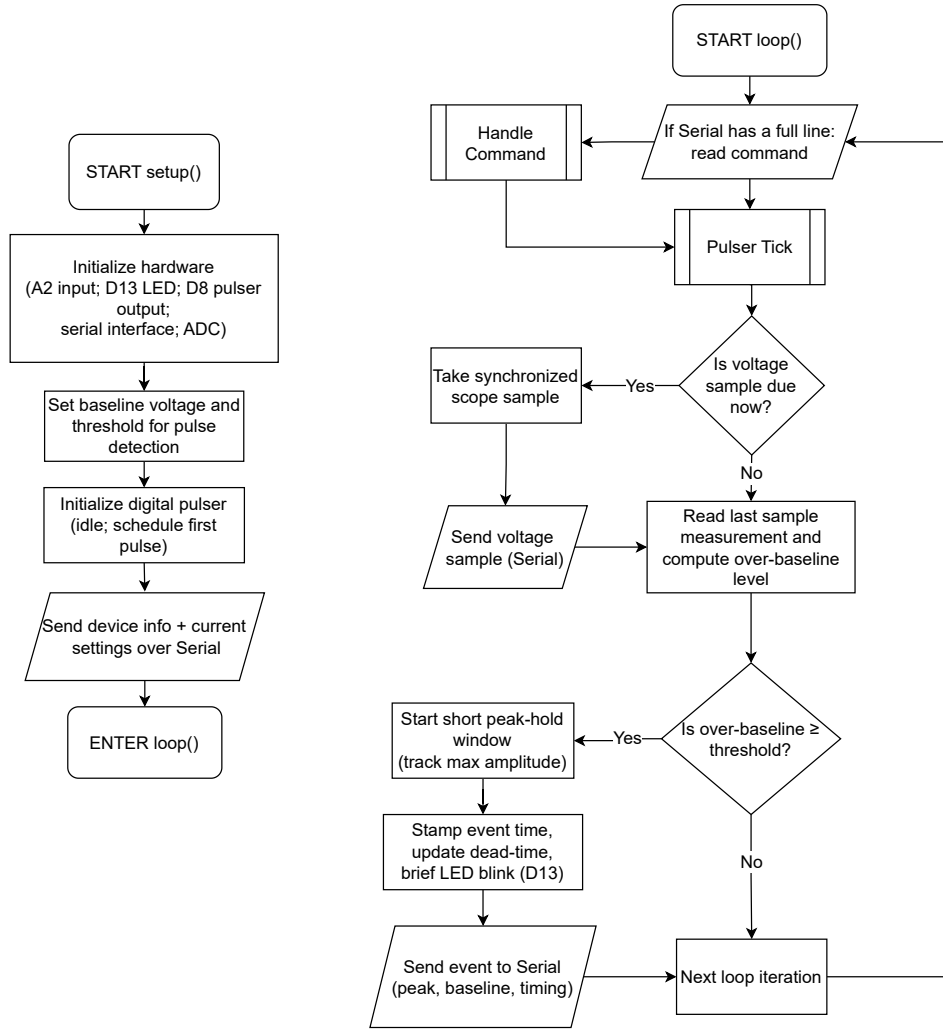


Figure 3.8: Simplified Arduino firmware logic flow.

This format was chosen for human readability and ease of parsing in Python. Runtime configuration commands (e.g., `SET THRESHOLD MV 50`) allow dynamic adjustment of thresholds or baseline levels without firmware re-flashing, improving test flexibility.

#### 3.4.4 Python Logger and GUI Design

The host-side acquisition and visualization software, implemented in Python, serves as both the control interface and logging system. It was designed around three guiding principles: (1) providing real-time insight through responsive graphical feedback, (2) ensuring reproducible, structured data storage, and (3) maintaining extensibility for future multi-detector or remote operation.



### Program Structure

The application is implemented as a single `Tkinter`-based program centered on the controller class `CR3DApp`, which manages all GUI components, serial communication, data queues, and session statistics. A lightweight auxiliary class, `RunningHist`, maintains a bounded histogram of recent event amplitudes for live estimation of mean peak voltage (MPV) and signal distribution.

Upon initialization, `CR3DApp` establishes a serial connection to the Arduino at 115200 baud and launches a background thread that continuously reads JSON-formatted messages (as defined in subsection 3.4.3). Incoming data objects are placed into a thread-safe queue, while a 1 ms GUI update loop retrieves these entries, applies local timestamps, updates the live plot, refreshes running statistics, and writes each record to a structured CSV log. This threaded architecture maintains responsiveness and synchronization throughout extended acquisition sessions, even under high event rates.

### GUI Layout and Design Philosophy

The GUI, implemented using `Tkinter` for portability and low overhead, adopts a single-window layout divided into three functional regions:

1. **Connection Panel:** manages serial port selection, session control, and live status indication.
2. **Plot Panel:** renders a continuously updating voltage–time plot using `matplotlib.animation`.
3. **Statistics Panel:** displays current acquisition metrics including event count, count rate (CPM), mean peak voltage (MPV), and estimated dead time.

The interface emphasizes clarity and situational awareness over visual complexity. All displayed metrics are derived directly from cumulative data streams, enabling the operator to monitor detector behavior and environmental influences in real time.

### Live Statistics and Data Logging

The application maintains continuously updated statistical summaries calculated from recent acquisition windows. Key quantities include:

### 3.4. FIRMWARE AND DATA-LOGGING SUBSYSTEM DESIGN

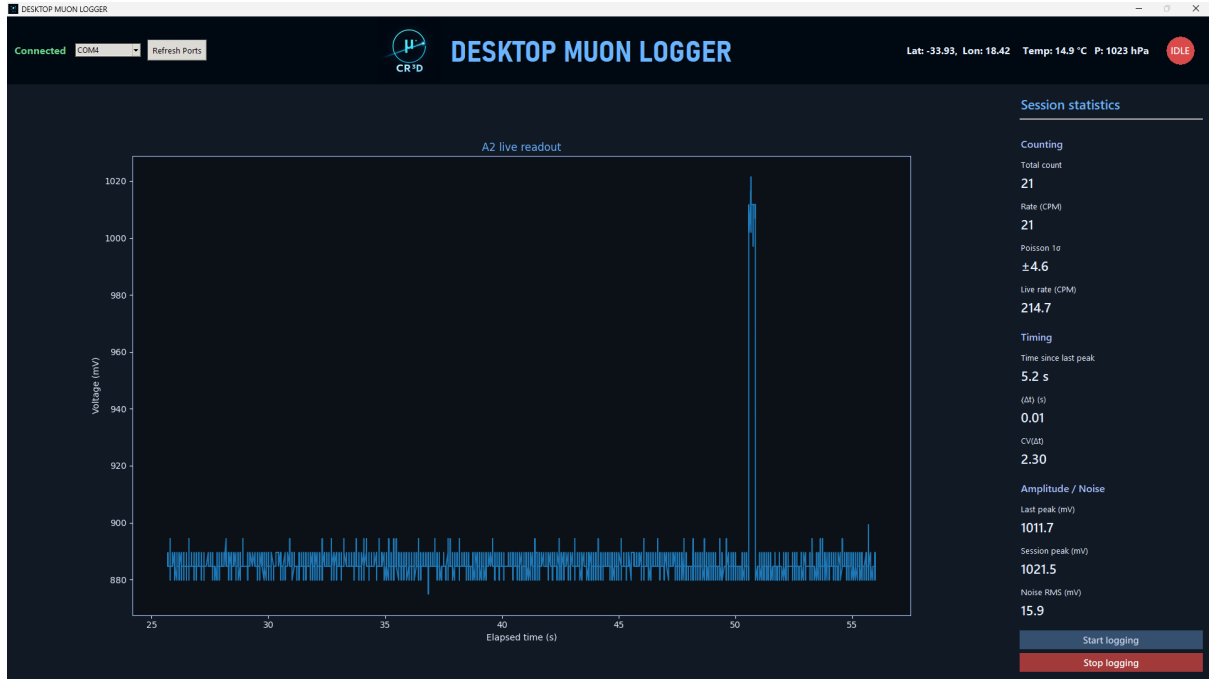


Figure 3.9: Layout of the `cr3d_logger.py` graphical interface.

- **Count rate (CPM):** number of detected events per minute.
- **Mean peak voltage (MPV):** rolling average of event amplitudes.
- **RMS noise:** baseline variability estimate from idle samples.
- **Environmental metadata:** location, temperature, and atmospheric pressure from the OpenMeteo API.

Each event is appended to a CSV file with standardized headers providing both detector and environmental context:

```
"timestamp_local","mv","adc","baseline_adc",  
"lat","lon","temp_C","pressure_hPa"
```

All sessions are automatically timestamped in their filenames for traceability. This enables later correlation between detector count rate and the environmental parameters relevant to cosmic-ray flux variation from literature [2].

### 3.4.5 Overall Subsystem Design

The firmware and data-logging subsystem was designed to form a robust, modular bridge between the AFE and the computational analysis environment. The Arduino firmware provides reliable, low-latency event serialization, while the Python GUI implements structured visualization and logging grounded in usability and reproducibility principles. Together, these elements round off a complete detector-to-data acquisition chain, verified through simulated and injected test signals and readily adaptable for full detector operation once the AFE and scintillator subsystems are overhauled with an actual scintillator-SiPM interface.

## 3.5 Conclusion of Design Methodology

This chapter established the complete methodological foundation for the detector’s design, detailing the theoretical models, analytical derivations, and subsystem architectures that collectively define the project framework. Through this structured approach, the simulation, analog, and digital domains were developed in parallel yet coherently, ensuring that the transition from physical modeling to signal processing was both traceable and technically consistent.

The design process demonstrated that a fully operational muon detection pipeline can be realized through a combination of theoretical modeling, circuit-level analysis, and modular software integration, even under severe practical constraints. Adaptation to challenge such as component failures, limited hardware access, and time restrictions was not peripheral but central to the design process itself. Each adjustment informed subsequent methodological choices, reinforcing the modular and simulation-driven character of the overall framework. As a result, simulation-based validation replaced full experimental prototyping, yet the resulting system architecture remains physically realizable and analytically sound.

Having established this integrated design, the next step is to verify its functional behaviour through controlled testing and simulation.

# Chapter 4

## Simulation/Design Testing and Results

This chapter describes how each of the detector subsystems designed in chapter 3 was tested and presents the results obtained from those tests.

### 4.1 Scintillator Simulation Subsystem

All tests of the scintillator simulation subsystem were performed within the **Geant4** environment using dedicated macro scripts. Each macro varied a single parameter of the simulation while all others were held constant, enabling isolated observation of its effect on the simulation outputs and whether they agree with the physical principles that govern scintillation interactions. For every run, the simulation produced both visual outputs of muon trajectories within the EJ-200 scintillator and CSV data files containing the relevant event quantities.

#### 4.1.1 Test 1: Scintillation Outputs vs. Muon Energy

In this test, the muon's incident position and trajectory were fixed while its kinetic energy was varied between 0.5 GeV and 5 GeV in discrete increments using the `/gun/energy` macro command.

## 4.1. SCINTILLATOR SIMULATION SUBSYSTEM

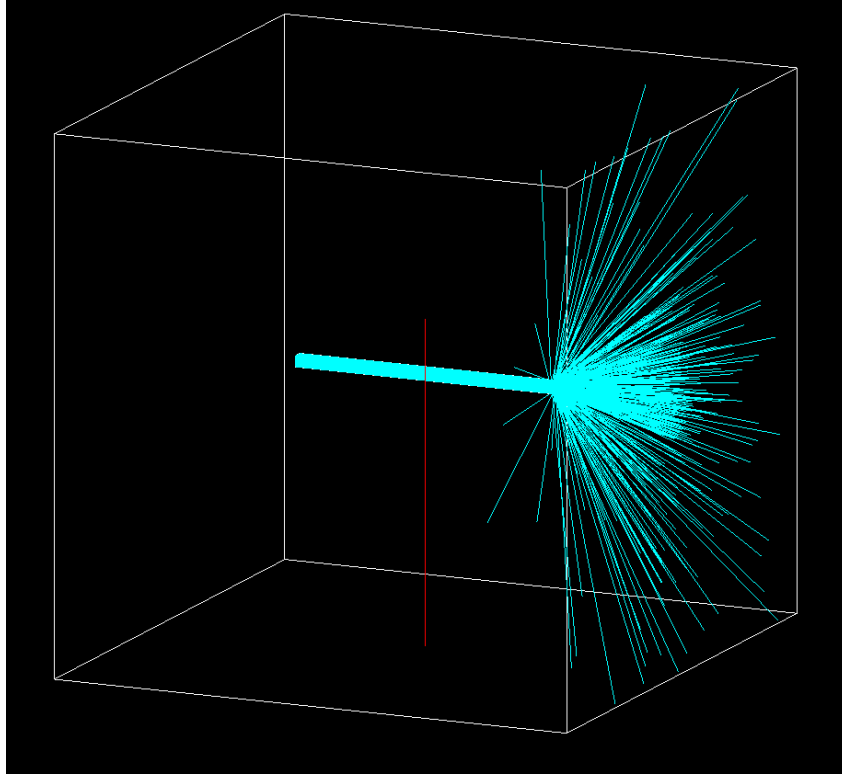


Figure 4.1: Visual output from Geant4 energy-sweep macro showing muon tracks (red) and scintillation photon emission (cyan) within the EJ-200 volume.

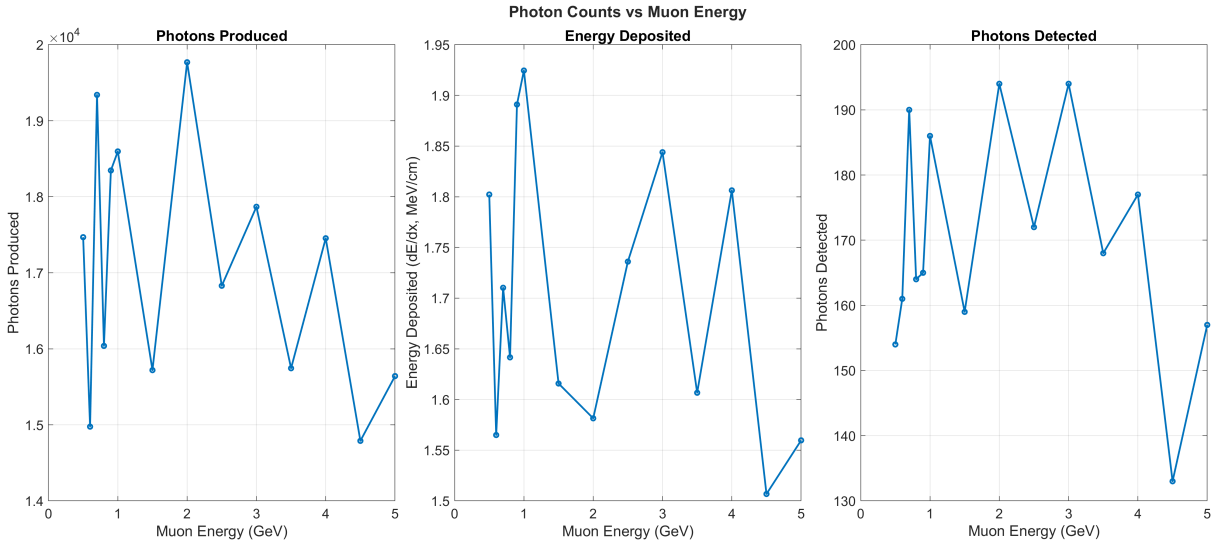


Figure 4.2: Simulation output showing relationship between muon energy and photons counts.

The resulting plot (Figure 4.2) presents the values of each recorded observable across the tested energy range.

### 4.1.2 Test 2: Scintillation Outputs vs. Muon Path Length

To examine the effect of muon trajectory on the scintillation simulation output, a second macro varied the entry angle of the muon through the center of the scintillator while maintaining a constant energy of 2 GeV. This produced a range of muon path lengths traveled through the scintillator, allowing the relationship between traversal distance and light yield to be evaluated.

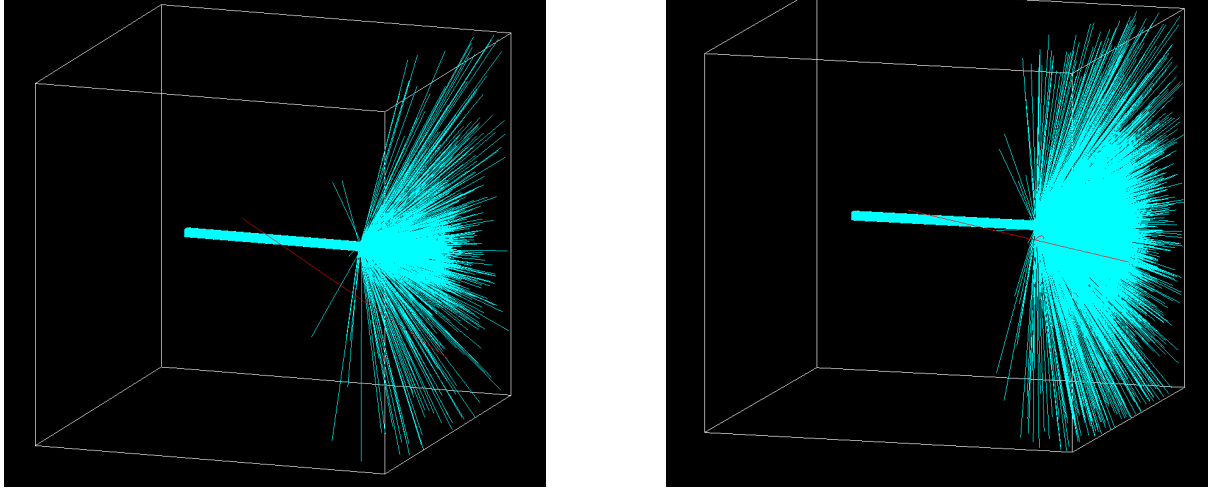


Figure 4.3: Visualization of muon trajectories producing different path lengths within the scintillator and its effect on photon yield.

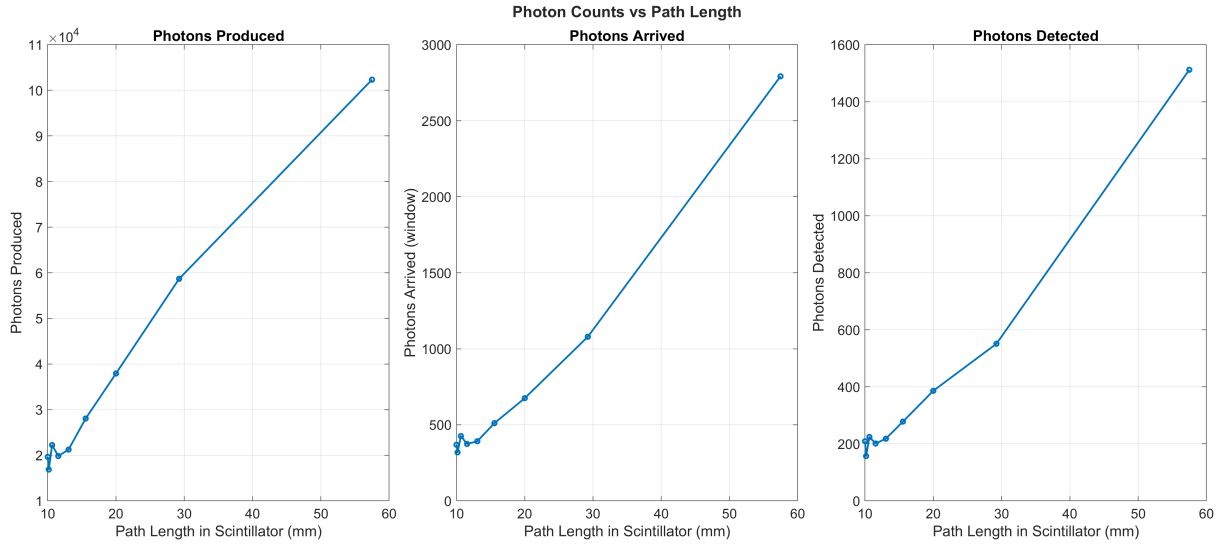


Figure 4.4: Simulation output showing relationship between muon path length and photons counts.

The CSV data collected from this sweep was aggregated to produce Figure 4.4, which plots the total emitted, arrived, and detected photons as a function of path length.

### 4.1.3 Test 3: Scintillation Outputs vs. Birks' Constant

A third macro investigated the effect of scintillator quenching on photon yield and whether it agrees with its governing physical principles by varying the Birks' constant ( $k_B$ ) parameter between 0.01 mm/MeV and 0.2 mm/MeV. All geometric and particle parameters were kept constant to isolate the influence of this quenching factor on simulated light output.

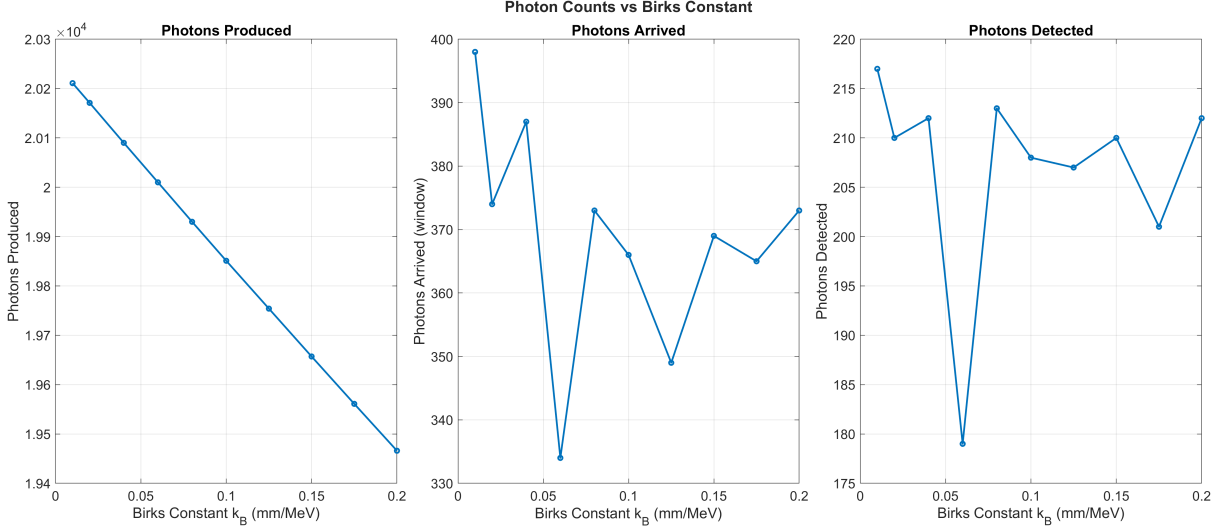


Figure 4.5: Variation of photon yield with Birks' constant over the range 0.01–0.20 mm/MeV.

The resulting plot (Figure 4.5) shows the relative change in emitted, arrived, and detected photons as a function of  $k_B$ .

## 4.2 Analog Front-End (AFE) Subsystem

Testing of the analog front-end subsystem comprised two stages: simulated current injection testing using LTSpice and hardware current injection testing using the physical prototype. Testing conditions using a voltage pulser from 0-5V and RC low-pass configuration with  $R_{pulse} = 5k\Omega$  and  $C_{pulse} = 22pF$  were replicated in both stages to ensure a fair scientific comparison of results. Both tests aimed to confirm that the circuit's transient and steady-state behavior matched the analytical performance derived in Chapter 3.

### 4.2.1 Simulated Circuit Testing

The AFE circuit was first tested in LTSpice using current injection pulses corresponding to the average SiPM output derived from the Geant4 simulations. The injected pulse due to current injection RC values had an amplitude of approximately 1 mA and duration of 55 ns, which corresponds to an SiPM pulse for roughly 180 photons detected. This was modeled after the typical photon yields of the scintillator simulation output.

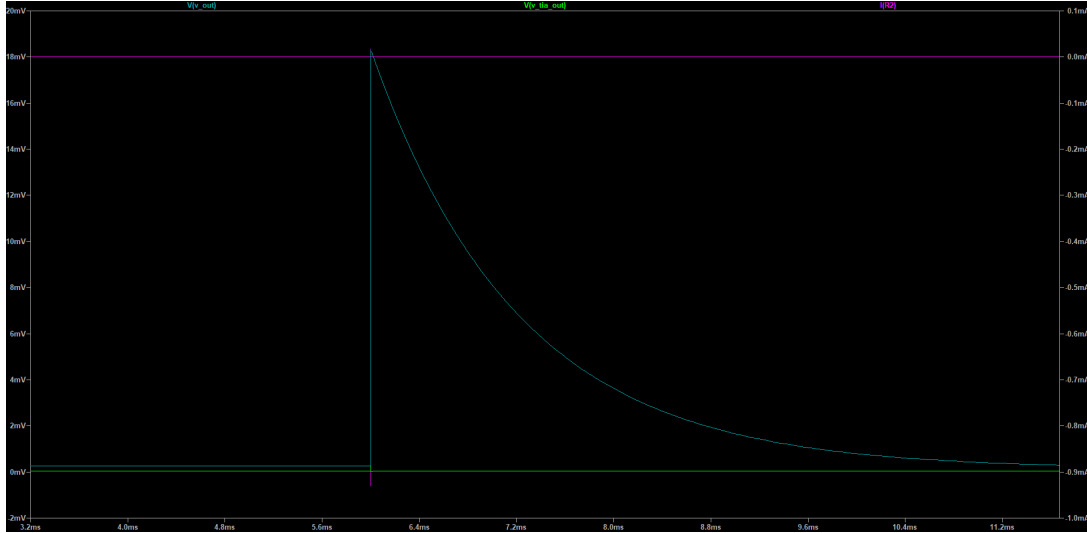


Figure 4.6: LTSpice transient simulation showing input current (pink), TIA output voltage (green), and final filtered output (cyan) of the AFE circuit.

### 4.2.2 Hardware Testing

The fabricated AFE prototype, powered from the Arduino Nano, was tested under the exact same RC current injection conditions using a pulse generator configured to replicate current pulses used in the LTSpice test. Oscilloscope measurements were taken at the TIA output and final filter output.

### 4.2.3 Acceptance Testing Results

Table 4.1 summarizes the outcomes of the acceptance tests defined in chapter 3. Each test was evaluated as either passed or failed based on the measured data of the AFE hardware testing.

All defined performance targets were met during hardware testing at varying degrees



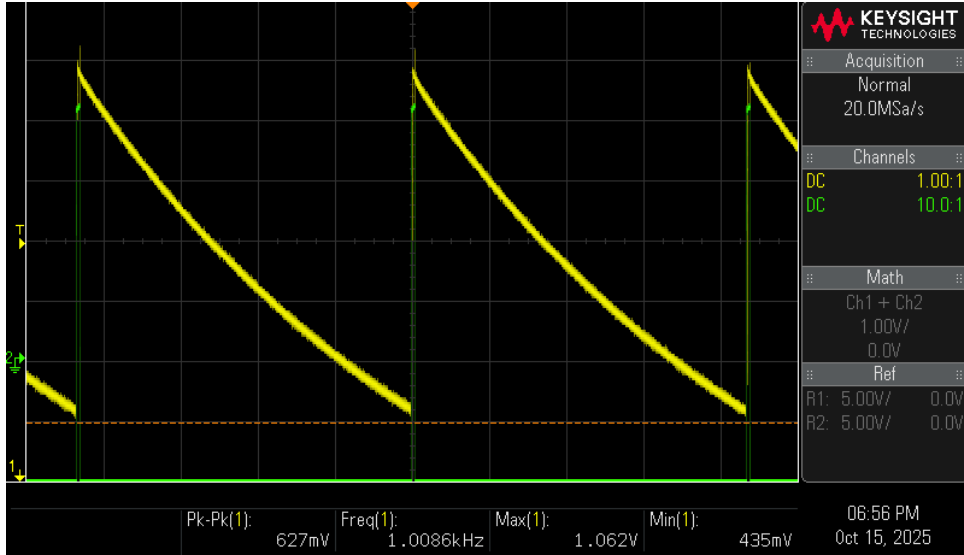


Figure 4.7: Oscilloscope capture of TIA output (green) and AFE output voltage (yellow).

Table 4.1: Acceptance test results for the AFE subsystem.

ID	Test Remarks	Result
AFE-1	Baseline RMS noise measured at 7mV under zero input current.	Pass
AFE-2	Measured decay constant of roughly 1.1ms.	Pass
AFE-3	Output voltage proportional to injected charge	Pass
AFE-4	No visible clipping or saturation of final stage output on 5V supply	Pass

of success, confirming that the AFE subsystem operated within its analytical design specifications.

### 4.3 Firmware and Data-Logging Subsystem

The firmware and data-logging subsystem was tested to ensure correct data capture, serial communication, live plotting, and file logging when interfaced with the AFE circuit.

### 4.3.1 Live Operation and Serial Communication

The Arduino Nano was programmed with the firmware designed in chapter 3. During testing, the device successfully detected injected pulse events and transmitted them via the serial interface to the Python logging application.

```
{
  "type": "sample",
  "ts_us": 10271840,
  "adc": 175,
  "mv": 855.33,
  "dht_C": null
}
{
  "type": "sample",
  "ts_us": 10277872,
  "adc": 174,
  "mv": 850.44,
  "dht_C": null
}
{
  "type": "sample",
  "ts_us": 10283912,
  "adc": 175,
  "mv": 855.33,
  "dht_C": null
}
{
  "type": "sample",
  "ts_us": 10289944,
  "adc": 175,
  "mv": 855.33,
  "dht_C": null
}
{
  "type": "sample",
  "ts_us": 10295976,
  "adc": 174,
  "mv": 850.44,
  "dht_C": null
}
{
  "type": "sample",
  "ts_us": 10302016,
  "adc": 175,
  "mv": 855.33,
  "dht_C": null
}
{
  "type": "sample",
  "ts_us": 10308060,
  "adc": 208,
  "mv": 1016.62,
  "dht_C": null
}
{
  "type": "event",
  "ts_us": 10318268,
  "adc_peak": 206,
  "mv_peak": 1006.84,
  "baseline_adc": 180,
  "dead_us": 5006504,
  "dht_C": null
}
{
  "type": "sample",
  "ts_us": 10323752,
  "adc": 175,
  "mv": 855.33,
  "dht_C": null
}
```

Figure 4.8: Example of live serial data stream showing alternating **sample** and **event** JSON messages received by the Python logger.

### 4.3.2 Graphical User Interface and Live Statistics

The `cr3d_logger.py` application was executed on the host computer to visualize live data from the Arduino. The interface correctly plotted the AFE output voltage in real time and updated both UI elements and event statistics, including count rate and mean peak voltage.

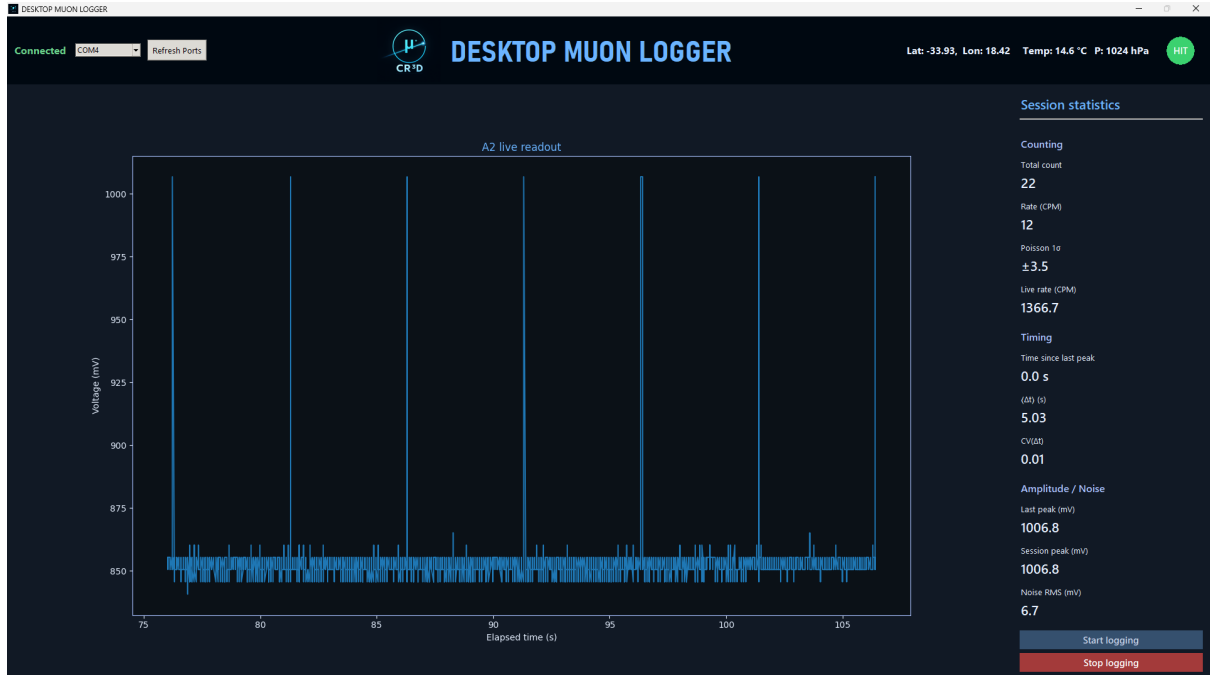


Figure 4.9: Graphical user interface of the Python data-logging application during active current-injection testing.

### 4.3.3 Data Logging and File Output Verification

All incoming serial data was successfully parsed and stored as timestamped CSV files on the host system. A representative extract of the logged dataset is shown in Table 4.2.

Table 4.2: Excerpt of recorded event data from logging subsystem.

Timestamp	Peak (mV)	ADC Value	Temp (°C)	Pressure (hPa)
2025-10-10 12:03:21.114	812.3	166	20.8	1012.1
2025-10-10 12:03:22.031	798.5	162	20.8	1012.0
2025-10-10 12:03:23.512	824.0	168	20.9	1012.0

The application maintained stable data streaming throughout extended acquisition sessions, confirming correct synchronization between firmware and host software.

# Chapter 5

## Discussion and Interpretation of Results

This chapter interprets the results presented in chapter 4, drawing connections between research, simulation, analytical design, and experimental testing outcomes.

### 5.1 Scintillator Simulation Subsystem

In general, the scintillation simulation performed exactly as expected and designed. The 3D visual outputs shown throughout section 4.1 clearly illustrates that muon incidence on the scintillator volume produces corresponding bursts of optical photons. These figures also confirm that the reflective wrapping was modeled correctly, as photons are internally reflected on all faces of the scintillator besides the face on which the SiPM window is placed. This behaviour validates the simulation’s generation of minimum-ionizing muon particles as well as optical photon production and tracking.

#### 5.1.1 Scintillation Outputs vs. Muon Energy

The photon yield results obtained from the **Geant4** simulation confirmed the expected plateau behaviour described by the Bethe–Bloch equation discussed in subsection 2.1.3. While photon yields were not perfectly constant between runs, this is to be expected due to factors such as internal reflection and absorption causing minor differences between

photon yield depending on their simulated trajectories for a given run. Figure 4.2 shows that for increasing muon kinetic energies, the amount of energy deposited by the muon never exceeds  $2 \text{ MeV } g^{-1}cm^2$ , consistent with the theoretical plateau quoted from literature in subsection 2.1.3.

At sub-GeV energies, the minor observed reduction in photon yield corresponds to the increased specific energy loss near the stopping power peak, a result in line with literature models of plastic scintillators. These agreements validate both the simulation geometry and the material parameters assigned to the EJ-200 scintillator in simulation, including its light yield and refractive properties.

### 5.1.2 Scintillation Outputs vs. Muon Path Length

The variation of photon yield with muon trajectory showed a strong near-linear scaling with track length inside the scintillator, seen in Figure 4.4. This behaviour indicates that optical losses were effectively minimized in the simulated geometry, and that total light production is dominated by volumetric energy deposition rather than surface effects. The 3D visualization of these tests confirmed that photon propagation was indeed configurable through macro commands, and that reflections were spatially uniform across the bar with minimal localized absorption or anomalous clustering near the SiPM window.

The observed correlation between path length and photon yield thus reinforces the validity of the geometry and supports the literature-informed assumption that scintillation light collection can be modeled as linearly dependent on deposited energy and muon path length.

### 5.1.3 Scintillation Outputs vs. Birks' Constant

When the Birks' constant was varied between 0.01 and 0.2 mm/MeV, a perfectly linear expected decrease in photon emission was observed, demonstrating correct implementation of scintillation quenching in the simulation as researched in subsection 2.1.3.

This sensitivity analysis confirmed that even moderate deviations in  $k_B$  significantly affect total light output. The consistency of this relationship with empirical quenching data from the EJ-200 studies and datasheets suggests that the selected default  $k_B$  value of 0.156 mm/MeV provides a suitable baseline for modeling realistic scintillator photons

yields.

## 5.2 Analog Front-End (AFE) Subsystem

### 5.2.1 Simulated Circuit Testing

The LTSpice transient simulation surprisingly did not follow the analytical derivations established in subsection 3.3.4. The TIA stage exhibited a 18 mV/mA transimpedance gain in response to injected current pulses, quite far from the derived 0.47 V/mA target in subsection 3.3.4. Despite this major discrepancy in gain, the peak-hold and RC filtering stages still managed to function as expected, extending transient signals into a roughly 3ms decay envelope suitable for ADC sampling. This time constant also did not match calculated expectations. The most likely explanation for these simulated responses not matching calculations is the fact that exact SPICE models for each op-amp and the Schottky diode were not able to be found, prompting the use of generic component models in the simulation. The parameters of these generic models were tuned to match each component's datasheet, but still produced unexpected results and over-idealized op-amp behaviour.

### 5.2.2 Hardware Testing

Fortunately, the physical prototype of the AFE subsystem performed much closer to its calculated expectations when subjected to identical current injection tests when powered by the 5V Arduino Nano supply. Shown in the oscilloscope plot in Figure 4.7, experimental current injection tests produced a transimpedance gain of 0.63 V/mA, slightly exceeding designed target but still producing a detectable voltage peak. The peak-hold stage captured these fast TIA peaks well, and the time constant was measured to be approximately 1.1ms, almost perfectly matching the derived 1.2ms time constant. It should be noted that the baseline voltage under no input current was 0.43V rather than 0V. This was expected due to the OPA656 used in the TIA stage not being a rail-to-rail op-amp and being unable to swing below this voltage. The RMS noise at the AFE subsystem's output was measured to be roughly 7mV both through oscilloscope measurements and measured by the firmware and data-logging subsystem. This resulted in clean, noise-free voltage signals at the AFE output, ideal for ADC data capture.

Overall, the physical AFE circuit performed exceptionally compared to its simulated counterpart. This led to all acceptance tests being passed, and validation of the circuit design justification and principles behind this subsystem’s development.

### 5.3 Firmware and Data-Logging Subsystem

#### 5.3.1 Live Operation and Serial Communication

The Arduino firmware demonstrated stable analog sampling and serial transmission at 115200 baud with no evidence of data loss during extended operation. The inclusion of structured JSON formatting correctly enabled reliable and unambiguous decoding by the Python logger, facilitating real-time visualization and statistical computation. When combined with the self-contained pulser function, this firmware provided a means to demonstrate and visualize AFE performance completely portably, supporting the desktop-based design philosophy for the project.

#### 5.3.2 Graphical User Interface and Live Statistics

The Python-based GUI exhibited consistent refresh behavior and responsive real-time plotting, even during high-rate simulated current injection. The running statistics proved accurate when compared to the known characteristics of the injected test pulses and voltage output. The interface successfully conveyed detector state, environmental context, and acquisition integrity at a glance, validating its design philosophy of operational clarity over visual complexity. These results affirm that the GUI effectively supports monitoring and diagnostic roles in future field operation scenarios.

#### 5.3.3 Data Logging and File Output Verification

Data captured by the Python logger were stored in structured CSV files with consistent headers and timestamp synchronization between host and device. Environmental metadata (temperature, pressure, and location) were correctly appended to each record, enabling later correlation with external conditions. The uniformity and completeness of the datasets confirm that the end-to-end software stack satisfies reproducibility and traceability

requirements essential for long-term muon flux monitoring if the system is later interfaced with a working SiPM and scintillator.

## 5.4 Overall Discussion and Evaluation

The scintillator simulation subsystem successfully achieved its objective of producing a physically representative model of scintillation light generation and transport within the EJ-200 medium. Through iterative parameter sweeps and macro-driven experimentation, it confirmed both the expected energy-loss plateau and the proportional dependence of photon yield on muon path length. These results validate the simulation’s geometry, material definitions, and optical processes, establishing a solid theoretical foundation for signal expectation in the downstream detector electronics.

The analog front-end (AFE) subsystem demonstrated that the design principles derived analytically in subsection 3.3.4 translate effectively into practice. Despite inaccuracies in the LTSpice simulation, the hardware implementation met or exceeded all key performance targets, achieving the intended gain, stability, and signal-to-noise ratio on a single 5 V supply. This confirmed that the AFE’s simplified yet robust topology was appropriate for clean signal acquisition from fast, low-amplitude SiPM pulses.

The firmware and data-logging subsystem completed the end-to-end functionality of the detector by reliably digitizing, streaming, and recording the AFE’s analog outputs. Its responsive GUI and structured logging demonstrated seamless synchronization between hardware and software, enabling real-time insight and traceable data storage.

Together, these results validate the detector’s overall architecture: a coherent, modular, and reproducible design that integrates simulation, electronics, and software into a unified experimental framework which remains analytically verified and ready for full operational testing once a functioning SiPM is reintroduced.



# Chapter 6

## Conclusions

This project set out to design and validate a compact, low-cost cosmic muon detector that could bridge theoretical particle-interaction physics and practical detector instrumentation. While the initial ambition of constructing a fully operational muon counter proved unrealistic within the 12-week timeframe and limited material resources, the deliberate revision of objectives in mid-project was decisive to its success.

### 6.1 Alignment with Revised Goals

The revised project objectives presented in Table 3.1 were all successfully achieved. The **scintillator simulation subsystem** fulfilled its role as a predictive model, quantitatively reproducing the real-world expected relationships between cosmic-ray muons and plastic scintillator interactions. These simulations supplied the physically meaningful optical parameters that directly informed the analog design process.

The **analog front-end (AFE)** subsystem translated these optical expectations into an electrical domain with ADC-measurable, low-noise performance. Through systematic analytical derivation, circuit simulation, and current-injection testing, the AFE design was validated as a robust, single-supply readout circuit capable of interpreting realistic scintillation pulse behavior. Although real scintillation tests could not be conducted, the agreement between theory, simulation, and hardware verification confirmed the soundness of the electronic design.

The **firmware and data-logging subsystem** completed the detection pipeline by

implementing a reliable, modular acquisition and visualization environment. Its ability to stream, plot, and store structured test data with environmental context demonstrated that the software architecture is ready for integration with a functional detector head in future work. The resulting end-to-end framework—spanning photon generation, signal transduction, and digital logging—thus satisfies every revised deliverable.

## 6.2 Methodological and Scientific Contributions

Beyond the technical outcomes, the project’s greatest contribution lies in its methodological rigor and adaptability. Each subsystem was developed according to a design philosophy rooted in physical modeling, validation, and reproducible implementation. The decision to pivot from empirical muon detection to a simulation-centered study transformed a hardware-limited prototype into a well-defined research framework that can be independently tested, extended, and replicated. This structured methodology exemplifies how complex muon detector systems can be deconstructed, modeled, and validated analytically even when full-scale experimentation is impractical.

Moreover, the integration of computational physics, analog circuit design, and software engineering within a unified data pipeline represents a compact yet comprehensive and logical approach to experimental instrumentation. By explicitly linking these traditionally separate domains, the project demonstrates that meaningful detector research can be undertaken at an educational or resource-constrained level without compromising scientific integrity.

## 6.3 Overall Conclusions

In conclusion, this study successfully demonstrated that:

- A validated **Geant4** model can serve as a credible substitute for early-stage experimental testing, providing physically accurate photon statistics for electronic design input.
- A single-supply analog front-end can achieve stable, low-noise response and reliable transient shaping using readily available components and analytical design principles.
- A lightweight Arduino firmware and Python-based GUI can provide real-time visualization, structured logging, and statistical insight suitable for future muon flux studies.

Together, these findings confirm that the project’s revised methodological approach not only ensured completion within its constraints but also produced a scalable, validated foundation for future muon detection experiments. The resulting Cosmic Ray Detector and Data Dispatcher (CR3D) system stands as a proof-of-concept framework for educational cosmic-ray research, awaiting only the integration of a functional SiPM–scintillator assembly for full empirical validation.

# Chapter 7

## Future Recommendations

The outcomes of this study provide a solid foundation for the continuation of the system’s development into a fully operational experimental instrument. Future work should focus on extending the present framework into a validated detection system through the following improvements:

- **Hardware optimization:** The analog front-end should be implemented on a professionally fabricated PCB to minimize parasitic coupling and facilitate proper SiPM integration.
- **Functional detector assembly:** Integration of a new SiPM–scintillator pair is the highest priority for enabling validation of simulation-derived photon yields and for calibrating the electronic response to real muon events.
- **Software and data acquisition:** The logging suite can be extended for multi-channel coincidence detection and remote synchronization between distributed detector nodes, supporting flux correlation studies similar to existing open-source desktop muon detectors.
- **Long-term operation:** The system should be deployed over extended time periods to evaluate atmospheric influences on muon flux.

Collectively, these future improvements create a clear path from the current simulation-verified prototype to a fully realized, field-deployable muon detection system. By building on the scientific rigor and modular architecture established in this work, future iterations can transform the framework into a validated, network-capable scientific and educational instrument.

# Bibliography

- [1] B. Rossi, *Cosmic rays.*, ser. McGraw-Hill paperbacks in physics. New York: McGraw-Hill, 1964.
- [2] S. Navas *et al.*, “Review of particle physics - chapter: Cosmic rays,” *Phys. Rev. D*, vol. 110, no. 3, 2024.
- [3] R. Blandford, P. Simeon, and Y. Yuan, “Cosmic ray origins: An introduction,” *Nuclear Physics B - Proceedings Supplements*, vol. 256-257, pp. 9–22, 2014, cosmic Ray Origin – Beyond the Standard Models. [Online]. Available: <https://www.sciencedirect.com/science/article/pii/S0920563214001960>
- [4] J. R. Winckler, “Primary cosmic rays,” *Radiation Research*, vol. 14, no. 5, pp. 521–539, 1961. [Online]. Available: <http://www.jstor.org/stable/3570895>
- [5] T. K. Gaisser, R. Engel, and E. Resconi, *Cosmic Rays and Particle Physics*, 2nd ed. Cambridge University Press, 2016.
- [6] S. Navas *et al.*, “Review of particle physics — chapter: Passage of particles through matter,” *Phys. Rev. D*, vol. 110, no. 3, 2024.
- [7] D. Reyna, “A simple parameterization of the cosmic-ray muon momentum spectra at the surface as a function of zenith angle,” 2006. [Online]. Available: <https://arxiv.org/abs/hep-ph/0604145>
- [8] N. Lesparre, D. Gibert, J. Marteau, Y. Déclais, D. Carbone, and E. Galichet, “Geophysical muon imaging: feasibility and limits,” *Geophysical Journal International*, vol. 183, no. 3, pp. 1348–1361, 12 2010. [Online]. Available: <https://doi.org/10.1111/j.1365-246X.2010.04790.x>
- [9] A. Lechner, “Particle interactions with matter,” *CERN Yellow Rep. School Proc.*, vol. 5, p. 47, 2018. [Online]. Available: <https://cds.cern.ch/record/2674116>

- [10] S. M. Tajudin, Y. Namito, T. Sanami, and H. Hirayama, “Response of plastic scintillator to gamma sources,” *Applied Radiation and Isotopes*, vol. 159, 2020. [Online]. Available: <https://www.sciencedirect.com/science/article/pii/S0969804319301034>
- [11] A. Tkaczyk, H. Saare, C. Ipbüker, F. Schulte, P. Mastinu, J. Paepen, B. Pedersen, P. Schillebeeckx, and G. Varasano, “Characterization of ej-200 plastic scintillators as active background shield for cosmogenic radiation,” *Nuclear Instruments and Methods in Physics Research Section A: Accelerators, Spectrometers, Detectors and Associated Equipment*, vol. 882, pp. 96–104, 2018. [Online]. Available: <https://www.sciencedirect.com/science/article/pii/S0168900217311774>
- [12] R. Hajima, “Status and perspectives of compton sources,” *Physics Procedia*, vol. 84, pp. 35–39, 2016. [Online]. Available: <https://www.sciencedirect.com/science/article/pii/S1875389216303029>
- [13] A. S. Ankney, T. J. Berguson, J. D. Borgardt, and R. T. Kouzes, “Muon fluence measurements for homeland security applications,” Pacific Northwest National Laboratory (PNNL), Richland, WA (US), Tech. Rep., 08 2010. [Online]. Available: <https://www.osti.gov/biblio/1002191>
- [14] H. Kolanoski and N. Wermes, *Particle detectors: fundamentals and applications*. Oxford University Press, 2020.
- [15] S. N. Axani, “The physics behind the cosmicwatch desktop muon detectors,” 2019. [Online]. Available: <https://arxiv.org/abs/1908.00146>
- [16] A. Lechmann, D. Mair, A. Ariga, T. Ariga, A. Ereditato, R. Nishiyama, C. Pistillo, P. Scampoli, F. Schlunegger, and M. Vladymyrov, “Muon tomography in geoscientific research – a guide to best practice,” *Earth-Science Reviews*, vol. 222, 2021. [Online]. Available: <https://www.sciencedirect.com/science/article/pii/S0012825221003433>
- [17] C. Slayman, *JEDEC Standards on Measurement and Reporting of Alpha Particle and Terrestrial Cosmic Ray Induced Soft Errors*. Boston, MA: Springer US, 2011, pp. 55–76. [Online]. Available: [https://doi.org/10.1007/978-1-4419-6993-4\\_3](https://doi.org/10.1007/978-1-4419-6993-4_3)
- [18] R. Baumann, “Soft errors in advanced computer systems,” *IEEE Design Test of Computers*, vol. 22, no. 3, pp. 258–266, 2005.
- [19] G. Blasse, “Scintillator materials,” *Chemistry of Materials*, vol. 6, no. 9, pp. 1465–1475, 1994. [Online]. Available: <https://doi.org/10.1021/cm00045a002>

- [20] S. Moser, W. Harder, C. Hurlbut, and M. Kusner, “Principles and practice of plastic scintillator design,” *Radiation Physics and Chemistry*, vol. 41, no. 1, pp. 31–36, 1993. [Online]. Available: <https://www.sciencedirect.com/science/article/pii/0969806X9390039W>
- [21] S. Axani, K. Frankiewicz, and J. Conrad, “The cosmicwatch desktop muon detector: a self-contained, pocket sized particle detector,” *Journal of Instrumentation*, vol. 13, no. 03, p. P03019, mar 2018. [Online]. Available: <https://doi.org/10.1088/1748-0221/13/03/P03019>
- [22] M. Yeh *et al.*, “A new water-based liquid scintillator and potential applications,” *Nuclear Instruments and Methods in Physics Research Section A: Accelerators, Spectrometers, Detectors and Associated Equipment*, vol. 660, no. 1, pp. 51–56, 2011. [Online]. Available: <https://www.sciencedirect.com/science/article/pii/S0168900211016615>
- [23] M. Wurm *et al.*, “The next-generation liquid-scintillator neutrino observatory lENA,” *Astroparticle Physics*, vol. 35, no. 11, pp. 685–732, 2012. [Online]. Available: <https://www.sciencedirect.com/science/article/pii/S0927650512000503>
- [24] M. J. Weber, “Inorganic scintillators: today and tomorrow,” *Journal of Luminescence*, vol. 100, no. 1, pp. 35–45, 2002. [Online]. Available: <https://www.sciencedirect.com/science/article/pii/S0022231302004234>
- [25] W. W. Moses, “Current trends in scintillator detectors and materials,” *Nuclear Instruments and Methods in Physics Research Section A: Accelerators, Spectrometers, Detectors and Associated Equipment*, vol. 487, no. 1, pp. 123–128, 2002, 3rd International Workshop on Radiation Imaging Detectors. [Online]. Available: <https://www.sciencedirect.com/science/article/pii/S0168900202009555>
- [26] S. Navas *et al.*, “Review of particle physics — chapter: Particle detectors at non-accelerator experiments,” *Phys. Rev. D*, vol. 110, no. 3, 2024.
- [27] T. Avgitas, F. Dogliotti, J.-C. Ianigro, and J. Marteau, “Prototype cherenkov detector characterization for muon tomography applications,” *Nuclear Physics B*, vol. 1006, p. 116645, 2024. [Online]. Available: <https://www.sciencedirect.com/science/article/pii/S0550321324002116>
- [28] A. Arefiev, S. Barsuk, M. Danilov, V. Eiges, B. Fominykh, Y. Gilitsky, F. Khasanov, T. Kvaratscheliia, L. Laptin, V. Tchoudakov, I. Tichomirov, M. Titov, Y. Zaitsev, M. Buchler, R. Harr, P. Karchin, S. Nam, and J. Shiu, “A gaseous muon detector at the hera-b experiment,” *IEEE Transactions on Nuclear Science*, vol. 48, no. 4, pp. 1059–1064, 2001.

- [29] S. V. Polyakov, “Photomultiplier tubes,” in *Single-Photon Generation and Detection*, ser. Experimental Methods in the Physical Sciences, A. Migdall, S. V. Polyakov, J. Fan, and J. C. Bienfang, Eds. Academic Press, 2013, vol. 45, pp. 69–82. [Online]. Available: <https://www.sciencedirect.com/science/article/pii/B9780123876959000032>
- [30] F. Acerbi and S. Gundacker, “Understanding and simulating sipms,” *Nuclear Instruments and Methods in Physics Research Section A: Accelerators, Spectrometers, Detectors and Associated Equipment*, vol. 926, pp. 16–35, 2019, silicon Photomultipliers: Technology, Characterisation and Applications. [Online]. Available: <https://www.sciencedirect.com/science/article/pii/S0168900218317704>
- [31] C. Hagmann, D. Lange, J. Verbeke, and D. Wright, “Cosmic-ray shower library (cry),” *Lawrence Livermore National Laboratory document UCRL-TM-229453*, 2012.
- [32] A. A. Alves, M. Reininghaus, A. Schmidt, R. Prechelt, and R. Ulrich, “CORSIKA 8—a novel high-performance computing tool for particle cascade monte carlo simulations,” in *EPJ Web of Conferences*, vol. 251. EDP Sciences, 2021.
- [33] S. Agostinelli *et al.*, “Geant4—a simulation toolkit,” *Nuclear Instruments and Methods in Physics Research Section A: Accelerators, Spectrometers, Detectors and Associated Equipment*, vol. 506, no. 3, pp. 250–303, 2003. [Online]. Available: <https://www.sciencedirect.com/science/article/pii/S0168900203013688>
- [34] J. Allison *et al.*, “Geant4 developments and applications,” *IEEE Transactions on Nuclear Science*, vol. 53, no. 1, pp. 270–278, 2006.
- [35] G. Battistoni *et al.*, “Overview of the FLUKA code,” *Annals of Nuclear Energy*, vol. 82, pp. 10–18, 2015, joint International Conference on Supercomputing in Nuclear Applications and Monte Carlo 2013, SNA + MC 2013. Pluri- and Trans-disciplinarity, Towards New Modeling and Numerical Simulation Paradigms. [Online]. Available: <https://www.sciencedirect.com/science/article/pii/S0306454914005878>
- [36] CosmicWatch, “Desktop muon detector v2 (github repository),” 2020. [Online]. Available: <https://github.com/spenceraxani/CosmicWatch-Desktop-Muon-Detector-v2>
- [37] CosmicPi, “Cosmic pi (github repository),” <https://github.com/CosmicPi>, 2016.
- [38] —, “Official cosmicpi website,” 2016. [Online]. Available: <http://cosmicpi.org>



- [39] Eljen Technology, *EJ-200, EJ-204, EJ-208, EJ-212 Plastic Scintillators Datasheet*, Eljen Technology, 2023. [Online]. Available: [https://eljentechnology.com/images/products/data\\_sheets/EJ-200\\_EJ-204\\_EJ-208\\_EJ-212.pdf](https://eljentechnology.com/images/products/data_sheets/EJ-200_EJ-204_EJ-208_EJ-212.pdf)
- [40] Broadcom Inc., *AFBR-S4N66P014M NUV-MT Silicon Photomultiplier Datasheet*, Broadcom Inc., 2023. [Online]. Available: [docs.broadcom.com/docs/AFBR-S4N66P014M-NUV-MT-Silicon-Photomultiplier](https://docs.broadcom.com/docs/AFBR-S4N66P014M-NUV-MT-Silicon-Photomultiplier)
- [41] onsemi, *C-Series Silicon Photomultipliers (SiPM) — Low-Noise, Blue-Sensitive*, Semiconductor Components Industries, LLC, February 2022. [Online]. Available: <https://www.onsemi.com/pdf/datasheet/microc-series-d.pdf>
- [42] Hamamatsu Photonics K.K., *MPPC S13360 Series — Multi-Pixel Photon Counters for Precision Measurement*, Hamamatsu Photonics K.K., July 2025. [Online]. Available: [https://www.hamamatsu.com/content/dam/hamamatsu-photonics/sites/documents/99\\_SALES\\_LIBRARY/ssd/s13360\\_series\\_kapd1052e.pdf](https://www.hamamatsu.com/content/dam/hamamatsu-photonics/sites/documents/99_SALES_LIBRARY/ssd/s13360_series_kapd1052e.pdf)
- [43] Texas Instruments, Inc., *OPA656: 550 MHz, Unity-Gain Stable, FET-Input Operational Amplifier*, Texas Instruments, February 2024. [Online]. Available: <https://www.ti.com/lit/ds/sbos196i/sbos196i.pdf>
- [44] —, *OPA657: 1.6 GHz, Low-Noise, FET-Input Operational Amplifier*, Texas Instruments, August 2015. [Online]. Available: <https://www.ti.com/lit/ds/symlink/opa657.pdf>
- [45] Analog Devices, Inc., *AD8065/AD8066: 145 MHz, Low Noise, Low Distortion, High Speed Op Amps*, Analog Devices, Inc., February 2016. [Online]. Available: [https://www.analog.com/media/en/technical-documentation/data-sheets/ad8065\\_8066.pdf](https://www.analog.com/media/en/technical-documentation/data-sheets/ad8065_8066.pdf)
- [46] Texas Instruments, Inc., *OPAx365: 50-MHz, Zero-Crossover, Low-Distortion, High-CMRR, Rail-to-Rail I/O, Single-Supply Operational Amplifiers*, Texas Instruments, May 2023. [Online]. Available: <https://www.ti.com/lit/ds/symlink/opa365.pdf>
- [47] —, *OPAx350: High-Speed, Single-Supply, Rail-to-Rail Operational Amplifiers (MicroAmplifier Series)*, Texas Instruments, December 2015. [Online]. Available: <https://www.ti.com/lit/ds/symlink/opa4350.pdf>
- [48] Microchip Technology, *MCP6021/1R/2/3/4: Rail-to-Rail Input/Output, 10 MHz Op Amps*, Microchip Technology, March 2017. [Online]. Available: <https://ww1.microchip.com/downloads/en/devicedoc/20001685e.pdf>

# Appendix A

## Additional Files

### A.1 GitHub Repository Link

A link to all the source code, simulation files, and PCB schematics for the entire project can be accessed [here](#).

## A.2 GA Appendix

GA	Requirement	Justification and section in the report
1	Problem-solving	I framed the challenge of developing a compact muon detector as a complex systems problem linking particle physics, analog electronics, and embedded computation. Despite the many obstacles that prevented the full realization of initial objectives, I was able to pivot project goals to develop a system that is a proof-of-concept framework for educational cosmic-ray research. Demonstrated in chapter 3, section 3.1, and discussed in chapter 5.
4	Investigations, experiments and data analysis	I employed a structured research workflow that combined particle physics modeling, circuit design, and experimental validation, all of which was meticulously informed by research. Quantitative data relationships were established to evaluate meeting the broad and non-obvious goals of the overall study. Evident in chapter 2 and chapter 3
5	Use of engineering tools	Selected and applied a comprehensive suite of modern engineering tools: Geant4 for particle physics simulations, LTSpice for analog simulation, KiCAD for PCB design, and Python programming for data acquisition and visualization. Shown in chapter 3 and chapter 4
6	Professional and technical communication (Long report)	Produced a clear, technically accurate, and academically structured report with traceable design reasoning, formatted figures, and IEEE referencing. Communicated progress and results effectively in written and oral form throughout development. Evident across chapters 2–6.
8	Individual work	Conducted all project stages independently with minimal external guidance, from literature review and simulation setup to programming implementation, while maintaining professional responsibility in lab safety and documentation. Collaboration was limited to consultation with physics staff for component access and verification. Demonstrated throughout the entire report.
9	Independent learning ability	Developed new competencies in astroparticle physics, high-precision analog circuit design, and high-quality PCB etching. Evident in chapter 2, subsection 3.3.5, and section 3.3.

## A.3 Use of Artificial Intelligence Tools

Artificial intelligence tools were used in a limited and supplementary capacity during the preparation of this report. Specifically, AI assistance (via OpenAI’s ChatGPT) was used for minor improvements to report writing clarity and argument structuring, debugging sections of C++ code, and verifying the report word count. All technical design work, analysis, and original writing were conducted independently by me. An example of usage includes submitting a short paragraph draft for rewording to improve conciseness and coherence, after which only argument-structuring edits were adopted without altering technical content or conclusions.

# Appendix B

## Addenda

### B.1 Ethics Form



---

## PRE-SCREENING QUESTIONNAIRE OUTCOME LETTER

STU-EBE-2025-PSQ001983

2025/08/20

Dear Zuhayr Halday,

Your Ethics pre-screening questionnaire (PSQ) has been evaluated by your departmental ethics representative. Based on the information supplied in your PSQ, it has been determined that you do not need to make a full ethics application for the research project in question.

You may proceed with your research project titled:

Cosmic Ray Detector and Data Dispatcher

Please note that should aspect(s) of your current project change, you should submit a new PSQ in order to determine whether the changed aspects increase the ethical risks of your project. It may be the case that project changes could require a full ethics application and review process.

Regards,

Faculty Research Ethics Committee

Figure B.1: eRA Ethics Approval Form